

# CO<sub>2</sub> doping of organic interlayers for perovskite solar cells

<https://doi.org/10.1038/s41586-021-03518-y>

Received: 19 December 2019

Accepted: 6 April 2021

Published online: 2 June 2021

 Check for updates

Jaemin Kong<sup>1</sup>, Yongwoo Shin<sup>2</sup>, Jason A. Röhr<sup>1</sup>, Hang Wang<sup>1</sup>, Juan Meng<sup>1</sup>, Yueshen Wu<sup>3</sup>, Adlai Katzenberg<sup>1</sup>, Geunjin Kim<sup>4</sup>, Dong Young Kim<sup>5</sup>, Tai-De Li<sup>6,7</sup>, Edward Chau<sup>1</sup>, Francisco Antonio<sup>8</sup>, Tana Siboonruang<sup>1</sup>, Sooncheol Kwon<sup>9</sup>, Kwanghee Lee<sup>10,11</sup>, Jin Ryoun Kim<sup>1</sup>, Miguel A. Modestino<sup>1</sup>, Hailiang Wang<sup>3</sup> & André D. Taylor<sup>1,8</sup>✉

In perovskite solar cells, doped organic semiconductors are often used as charge-extraction interlayers situated between the photoactive layer and the electrodes. The π-conjugated small molecule 2,2',7,7'-tetrakis[N,N-di(4-methoxyphenyl)amino]-9,9-spirobifluorene (spiro-OMeTAD) is the most frequently used semiconductor in the hole-conducting layer<sup>1–6</sup>, and its electrical properties considerably affect the charge collection efficiencies of the solar cell<sup>7</sup>. To enhance the electrical conductivity of spiro-OMeTAD, lithium bis(trifluoromethane)sulfonimide (LiTFSI) is typically used in a doping process, which is conventionally initiated by exposing spiro-OMeTAD:LiTFSI blend films to air and light for several hours. This process, in which oxygen acts as the p-type dopant<sup>8–11</sup>, is time-intensive and largely depends on ambient conditions, and thus hinders the commercialization of perovskite solar cells. Here we report a fast and reproducible doping method that involves bubbling a spiro-OMeTAD:LiTFSI solution with CO<sub>2</sub> under ultraviolet light. CO<sub>2</sub> obtains electrons from photoexcited spiro-OMeTAD, rapidly promoting its p-type doping and resulting in the precipitation of carbonates. The CO<sub>2</sub>-treated interlayer exhibits approximately 100 times higher conductivity than a pristine film while realizing stable, high-efficiency perovskite solar cells without any post-treatments. We also show that this method can be used to dope π-conjugated polymers.

A conventional perovskite solar cell contains an active perovskite layer sandwiched between electron- and hole-transporting layers (ETLs and HTLs), which are essential for charge selectivity (Fig. 1a). Spiro-OMeTAD paired with LiTFSI is typically used as the HTL (Fig. 1b), in which LiTFSI is added as a dopant and radical cation stabilizer<sup>8</sup>; however, the doping process is typically initiated by exposing the pristine spiro-OMeTAD:LiTFSI film to air and light. Oxygen (O<sub>2</sub>), the actual dopant, oxidizes the spiro-OMeTAD film while LiTFSI mediates the reaction between O<sub>2</sub> and spiro-OMeTAD under illumination, producing a TFSI-stabilized radical cation along with lithium oxides<sup>9</sup> according to the following reactions: (i) spiro-OMeTAD + O<sub>2</sub> ↔ spiro-OMeTAD<sup>+</sup>O<sub>2</sub><sup>·-</sup>; and (ii) spiro-OMeTAD<sup>+</sup>O<sub>2</sub><sup>·-</sup> + LiTFSI → spiro-OMeTAD<sup>++</sup>TFSI<sup>-</sup> + Li<sub>x</sub>O<sub>y</sub>. Doubly oxidized spiro-OMeTAD species can also form during the reaction and act as a dopant to neutral spiro-OMeTAD, producing two singly oxidized spiro-OMeTAD molecules<sup>11</sup>. These conventional oxidation processes rely on very slow O<sub>2</sub> ingress into and diffusion through spiro-OMeTAD:LiTFSI, which usually takes between several hours and one day, and is dependent on the ambient conditions. Furthermore, these processes can result in unreacted reactants

and/or detrimental by-products remaining in the doped spiro-OMeTAD layer<sup>12,13</sup>.

## Pre-fabrication doping and CO<sub>2</sub>-doping mechanism

To avoid post-processing exposure of the pristine spiro-OMeTAD:LiTFSI film, we demonstrate a method to pre-dope spiro-OMeTAD molecules by bubbling the spiro-OMeTAD:LiTFSI solution with O<sub>2</sub> or carbon dioxide (CO<sub>2</sub>) for one minute (Fig. 1c). During the bubbling process, ultraviolet light—at a wavelength of around 365 nm and a corresponding energy of 3.4 eV, which is above the band gap of spiro-OMeTAD at approximately 3 eV—initiates the doping process by photoexciting the spiro-OMeTAD molecules in solution. The solution bubbled with O<sub>2</sub> exhibited relatively weak polaron absorption peaks centred at about 500 nm and about 1,600 nm (Fig. 1d), which are known to arise in oxidized spiro-OMeTAD<sup>8</sup>. Polaron-induced exciton quenching via charge transfer and/or Förster resonance energy transfer was observed from photoluminescence data (Fig. 1e), as expected<sup>14</sup>. Like O<sub>2</sub>, CO<sub>2</sub> is expected to act as a dopant in the pre-doping process, because

<sup>1</sup>Department of Chemical and Biomolecular Engineering, New York University Tandon School of Engineering, New York, NY, USA. <sup>2</sup>Advanced Materials Laboratory, Samsung Semiconductor, Inc., Cambridge, MA, USA. <sup>3</sup>Department of Chemistry, Yale University, New Haven, CT, USA. <sup>4</sup>Division of Advanced Materials, Korea Research Institute of Chemical Technology (KRICT), Daejeon, Republic of Korea. <sup>5</sup>Samsung Advanced Institute of Technology, Samsung Electronics, Suwon, Republic of Korea. <sup>6</sup>Advanced Science Research Center, The Graduate Center of the City University of New York, New York, NY, USA. <sup>7</sup>Department of Physics, City College of New York, New York, NY, USA. <sup>8</sup>Department of Chemical and Environmental Engineering, Yale University, New Haven, CT, USA. <sup>9</sup>Department of Carbon Convergence Engineering, Wonkwang University, Iksan, Republic of Korea. <sup>10</sup>Heeger Center for Advanced Materials (HCAM), Gwangju Institute of Science and Technology (GIST), Gwangju, Republic of Korea. <sup>11</sup>Research Institute for Solar and Sustainable Energies (RISE), Gwangju Institute of Science and Technology (GIST), Gwangju, Republic of Korea. <sup>✉</sup>e-mail: andre.taylor@nyu.edu

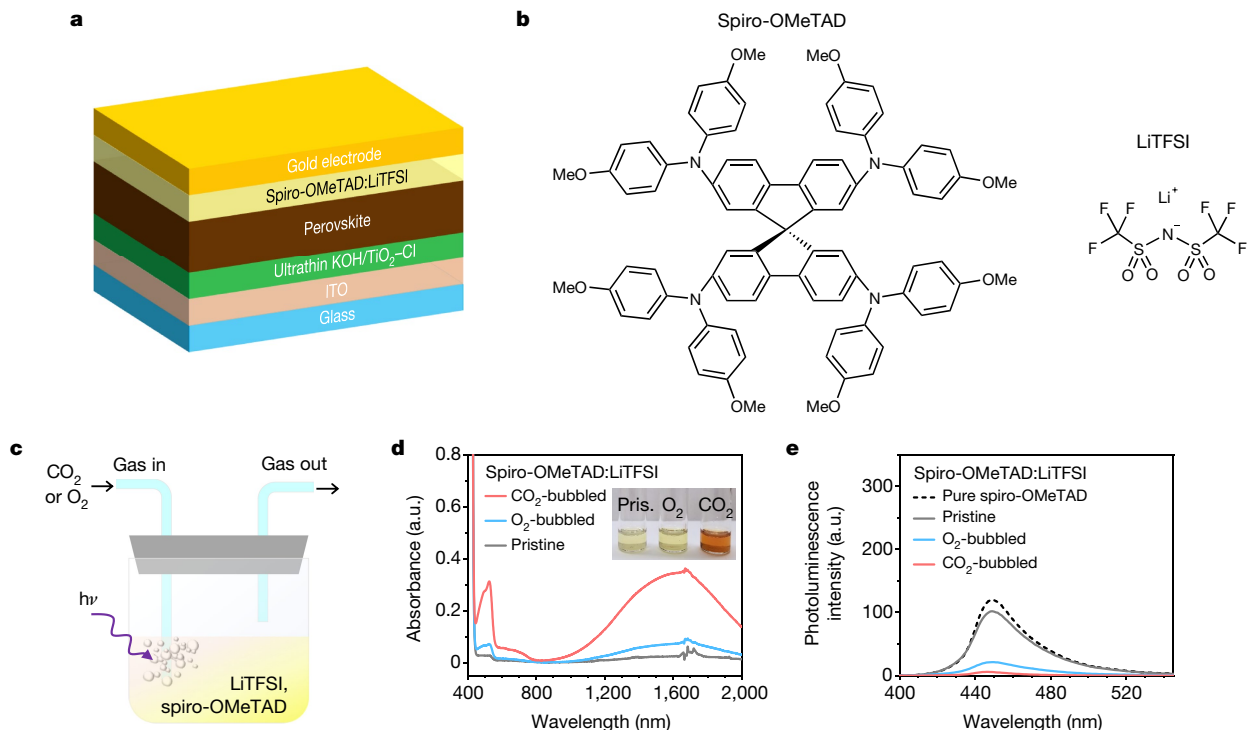


**Fig. 1 | Gas-assisted doping of the hole-conducting material and optical properties of reaction products.** **a**, Structure of a conventional perovskite solar cell device consisting of a transparent conductive oxide, ITO; the ETL,  $\text{TiO}_2\text{-Cl}$ , and an ultrathin layer of KOH; the active perovskite layer,  $\text{Cs}_{0.05}\text{FA}_{0.81}\text{MA}_{0.14}\text{PbI}_{2.55}\text{Br}_{0.45}$  (FA, formamidinium; MA, methylammonium); the HTL, a blend of spiro-OMeTAD and LiTFSI; and a top metal contact, Au. **b**, Molecular structures of spiro-OMeTAD and LiTFSI. **c**, Schematic of the gas bubbling process. While  $\text{O}_2$  or  $\text{CO}_2$  is blown into the spiro-OMeTAD:LiTFSI blend solution,

UV light ( $h\nu$ ) is shone into the solution. The processing time is 1 min. **d**, Ultraviolet-visible-near-infrared (UV-Vis-NIR) absorption spectra of pristine,  $\text{O}_2$ -bubbled and  $\text{CO}_2$ -bubbled spiro-OMeTAD:LiTFSI solutions. The inset shows photographs of the solutions. **e**, Photoluminescence spectra of a pure spiro-OMeTAD solution and of the spiro-OMeTAD:LiTFSI blends. The formation of polaron peaks and quenching of the photoluminescence are indicators of successful doping. a.u., arbitrary units.

the lowest unoccupied molecular orbital (LUMO) of spiro-OMeTAD ( $-2.05 \text{ eV}$ )<sup>15–17</sup> lies above the reduction potential for the reaction of  $\text{CO}_2$  to  $\text{CO}_2^{\cdot-}$  (standard reduction potential  $E^\circ = -1.90 \text{ V}$  versus standard hydrogen electrode (SHE))<sup>18–20</sup> (Extended Data Fig. 1a). Bubbling the solution with  $\text{CO}_2$  results in similar changes in the absorption and photoluminescence spectra as with  $\text{O}_2$ , with even more pronounced polaron peaks<sup>8,9</sup> (apparent colour change is shown in the inset of Fig. 1d) and photoluminescence quenching (Fig. 1e). Thus, we expect a greater number of oxidized spiro-OMeTAD molecules present in the  $\text{CO}_2$ -bubbled solution as compared to the  $\text{O}_2$ -bubbled solution<sup>21</sup>.

Density functional theory (DFT) calculations suggest that the new peaks observed in the experimental absorption spectra are indeed attributed to optical transitions from the lower energy levels to either a singly occupied molecular orbital (polaron state  $\text{P}^+$ ) or a fully empty state in the highest occupied molecular orbital (HOMO) (polaron state  $\text{P}^{2+}$ ) of the oxidized spiro-OMeTAD (Fig. 2a, b). In the calculated absorption spectrum of pure spiro-OMeTAD, only one prominent peak was found at around 350 nm (Fig. 2b), which corresponds to the HOMO to LUMO ( $E_\text{H} \rightarrow E_\text{L}^*$ ) transition (Fig. 2a). Spiro-OMeTAD with a single positive charge has a singly occupied molecular orbital that enables optical transitions from lower levels; the  $E_{\text{H}-2} \rightarrow E_\text{H}^{\text{P}^+}$  transition is shown to be responsible for the absorption at around 1,600 nm and the  $E_{\text{H}-3} \rightarrow E_\text{H}^{\text{P}^+}$  transition for absorption at around 700 nm (which probably corresponds to the peak observed at 500 nm in the experimental spectrum). Spiro-OMeTAD with charge of +2 has a fully empty state in its HOMO, and transitions from  $E_{\text{H}-2} \rightarrow E_\text{H}^{\text{P}^{2+}}$  and  $E_{\text{H}-3} \rightarrow E_\text{H}^{\text{P}^{2+}}$  are possible, seen as new absorption peaks at around 1,300 nm and around 700 nm, respectively, in the calculated absorption spectrum. Although the positions of the absorption peaks in the measured absorption spectrum of the  $\text{CO}_2$ -bubbled solution are slightly different to those in the calculated

spectra, we estimate that the two new peaks observed in the doped states are attributed to polarons formed in the oxidized spiro-OMeTAD.

Assuming that the  $\text{CO}_2$ -bubbled spiro-OMeTAD solution contains both oxidized forms, spiro-OMeTAD(TFSI) and spiro-OMeTAD(TFSI)<sub>2</sub>, the measured absorption spectrum (Fig. 1d) could be a superposition of two spectra (Fig. 2b). Because spiro-OMeTAD<sup>•2+</sup> diradical dication can oxidize neutral spiro-OMeTAD molecules, most of the doubly oxidized species will be reduced, producing two moles of spiro-OMeTAD<sup>+</sup>. On the basis of published protocols<sup>22</sup>, we estimate that 5.7 mol% of spiro-OMeTAD<sup>•2+</sup> will be formed during the  $\text{CO}_2$ -bubbling process (Extended Data Fig. 2a, b). Calculated from the equilibrium constant<sup>11</sup>, 98.95% of 5.7 mol% spiro-OMeTAD<sup>•2+</sup> (that is, 5.64 mol%) will produce a total of 11.27 mol% of spiro-OMeTAD<sup>+</sup>, leaving 0.06 mol% dications. The majority of the reaction product will therefore be singly oxidized species and might account for the measured absorption spectrum. From the mole fraction calculations, we estimate that the total doping efficiency is approximately 11.33%, which is similar to efficiencies reported in the literature<sup>11,22</sup>.

Because reaction rates are largely associated with reactant concentrations, the higher doping efficiency of  $\text{CO}_2$  could be attributed to the higher solubility of  $\text{CO}_2$  (molar fraction  $9.84 \times 10^{-3}$ ) in chlorobenzene at room temperature—an order of magnitude higher<sup>23–25</sup> than that of  $\text{O}_2$  ( $7.79 \times 10^{-4}$ ). In addition, the reduction of  $\text{CO}_2^{\cdot-}$  to C is energetically more favourable than that of  $\text{O}_2^{\cdot-}$  to  $\text{O}^{2-}$  (refs. <sup>26,27</sup>), meaning that  $\text{CO}_2$  doping has faster kinetics (Extended Data Fig. 1b, c). Considering that the reduction potential of  $\text{CO}_2^{\cdot-}/\text{Li}_2\text{CO}_3$  is  $+4.96 \text{ V}$ , and the HOMO of a neutral spiro-OMeTAD molecule is at  $+0.63 \text{ V}$  (Extended Data Fig. 1a),  $\text{CO}_2^{\cdot-}$  radicals can directly oxidize neutral spiro-OMeTAD molecules. This, as well as  $\text{CO}_2$  being more soluble than  $\text{O}_2$  in chlorobenzene, favours the oxidative  $\text{CO}_2$  reaction.

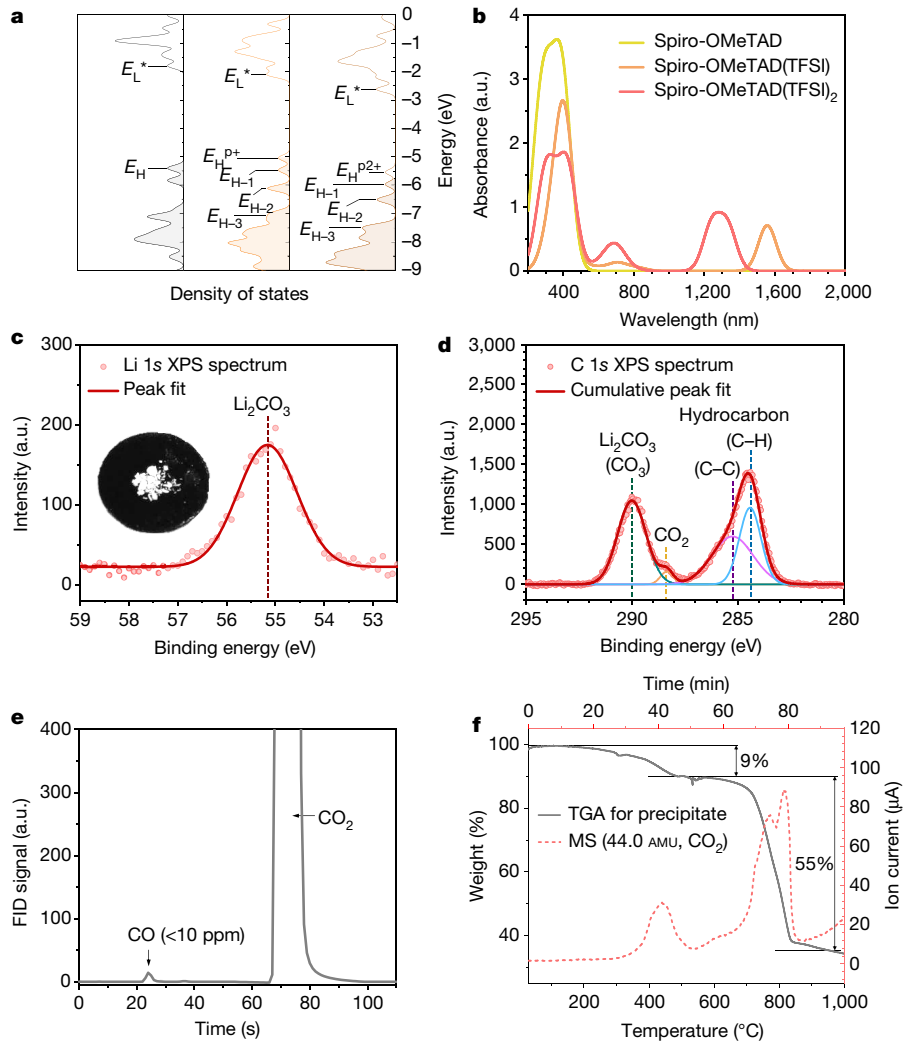


**Fig. 2 | Electronic structures of pristine and doped spiro-OMeTAD, and analysis of the precipitate produced during the  $\text{CO}_2$ -assisted doping process.** **a**, Electronic structure calculations for undoped spiro-OMeTAD (left) and spiro-OMeTAD with charges of either +1 (middle) or +2 (right) (spiro-OMeTAD(TFSI) and spiro-OMeTAD(TFSI)<sub>2</sub>, respectively). Here, we selected the ionization potential of the pristine system (−5.394 eV) as the reference HOMO level. The labels represent energy states that contribute to the absorption spectrum. **b**, Calculated absorption spectra of undoped spiro-OMeTAD and

oxidized spiro-OMeTAD. **c, d**, Li 1s XPS spectrum (**c**) and C 1s XPS spectrum (**d**) of the collected precipitate obtained by filtering the  $\text{CO}_2$ -bubbled solution. The precipitate, a white powder, is shown in the inset of **c**. **e**, GC-FID analysis of a gas sample taken from the headspace of the reaction vial. Only trace amounts of CO are found in the gas after the reaction; it consists mostly of  $\text{CO}_2$ . **f**, TGA–MS data for the precipitate. During the temperature-dependent decomposition of the precipitate, evolution of  $\text{CO}_2$  was detected in the weight-loss regions. AMU, atomic mass units.

Concomitant with the oxidation of spiro-OMeTAD molecules is the reduction of  $\text{O}_2$  and  $\text{CO}_2$ . In the  $\text{O}_2$ -bubbled solution, lithium oxides are expected to form after the oxidative reaction<sup>9,28–30</sup> according to the following equations:  $\text{Li}^+ + \text{O}_2 + \text{e}^- \rightarrow \text{LiO}_2$ ; or  $2\text{Li}^+ + \text{O}_2 + 2\text{e}^- \rightarrow \text{Li}_2\text{O}_2$ . However, no sediments were found, and filtering the solution with a PTFE membrane filter of pore size 0.22  $\mu\text{m}$  did not yield any measurable precipitate. This might be attributed to the formation of negligible amounts of  $\text{Li}_2\text{O}_2$ , and/or precipitates that are smaller than the filter pores. In the  $\text{CO}_2$ -bubbled solution, a sediment was formed and was collected by filtration. X-ray photoelectron spectroscopy (XPS) measurements revealed that the precipitate contained  $\text{Li}_2\text{CO}_3$  (binding energy 55 eV), as indicated in the Li 1s XPS spectrum (Fig. 2c). This was also confirmed by a carbonate signal (290 eV) in the C 1s XPS spectrum<sup>31,32</sup> (Fig. 2d). The peak at a binding energy of 228.4 eV was assigned either to chemisorbed  $\text{CO}_2^{*}$  (ref. <sup>32</sup>), originating from reaction intermediates or as a result of incomplete reaction, or to linear  $\text{CO}_2$  (ref. <sup>33</sup>) that was physisorbed from the atmosphere during sample preparation. Bubbling with  $\text{CO}_2$  under UV light might therefore generate  $\text{Li}_2\text{CO}_3$ , according to the reaction<sup>34</sup>:  $4\text{Li}^+ + 3\text{CO}_2 + 4\text{e}^- \rightarrow 2\text{Li}_2\text{CO}_3 + \text{C}$ . Peaks at 285.2 eV

(C–C) and 284.4 eV (C–H) in the C 1s XPS spectrum are attributed to remaining reactants and/or products such as neutral spiro-OMeTAD and/or oxidized spiro-OMeTAD salts. Although the precipitate was thoroughly rinsed with chlorobenzene and acetonitrile, it is possible that some reactants and/or products remained in the precipitate (Supplementary Fig. 1). In addition, because the reaction of Li ions with  $\text{CO}_2$  radical anions can produce carbon species (according to the equation  $4\text{Li}^+ + 3\text{CO}_2 + 4\text{e}^- \rightarrow 2\text{Li}_2\text{CO}_3 + \text{C}$ ), the C–C and C–H peaks observed in the C 1s XPS spectrum could also arise from these carbon products. An additional precipitation reaction might also be possible<sup>35</sup>:  $2\text{Li}^+ + 2\text{CO}_2 + 2\text{e}^- \rightarrow \text{Li}_2\text{CO}_3 + \text{CO}$ ; however, we detected only a trace amount of CO (<10 ppm) using gas chromatography with flame ionization detection (GC-FID) (Fig. 2e). We therefore conclude that this was not the main reaction that led to the formation of  $\text{Li}_2\text{CO}_3$ ; even if this reaction did occur, the evolved CO gas could react with  $\text{Li}^+$  ions in solution, producing  $\text{Li}_2\text{CO}_3$  and C (ref. <sup>36</sup>):  $3\text{CO} + 2\text{Li}^+ + 2\text{e}^- \rightarrow \text{Li}_2\text{CO}_3 + 2\text{C}$  (free energy of reaction at 298 K,  $\Delta G_{\text{rxn}} = -720.5 \text{ kJ mol}^{-1}$ ).

From thermogravimetric analysis coupled with online mass spectrometry (TGA–MS), we acquired more quantitative information about



**Fig. 3 | The proposed doping and precipitation reaction.** **a**, Spiro-OMeTAD and LiTFSI are mixed in chlorobenzene. **b**, The spiro-OMeTAD:LiTFSI blend is bubbled with  $\text{CO}_2$  under UV light. The photoexcited electrons in the spiro-OMeTAD are transferred to the dissolved  $\text{CO}_2$  gas, and the negatively charged  $\text{CO}_2$  will react with lithium ions, producing  $\text{Li}_2\text{CO}_3$  and carbon species. **c**, The

oxidized spiro-OMeTAD is stabilized by  $\text{TFSI}^-$ , resulting in p-type doping. The insets of each panel represent the electron wavefunction probability of the HOMO energy level; green and yellow isosurfaces indicate different phases (isosurface value of  $\pm 0.01 \text{ \AA}^{-3/2}$ ).

the precipitate. To avoid any unexpected oxidation, we conducted the precipitation decomposition experiments in an inert argon atmosphere (up to  $1,000^\circ\text{C}$ ). Two distinctive weight losses were observed at  $250\text{--}500^\circ\text{C}$  and at  $700\text{--}850^\circ\text{C}$ , corresponding to the two temperature ranges in which  $\text{CO}_2$  evolution was detected (Fig. 2f). The  $\text{CO}_2$  evolution observed in the lower temperature region ( $250\text{--}500^\circ\text{C}$ ) was most likely due to the decomposition of residual organic reactants and/or products in the precipitate and/or a release of  $\text{CO}_2$  from physisorbed or lithium carboxylic species from the reaction between  $\text{CO}_2^{+}$ ,  $\text{Li}^+$  and solvents<sup>37</sup>. By comparing the generated product with pure  $\text{Li}_2\text{CO}_3$ , we determined that the  $\text{CO}_2$  evolution observed in the higher temperature range ( $700\text{--}850^\circ\text{C}$ ) probably resulted from decomposition of the  $\text{Li}_2\text{CO}_3$  product (Supplementary Fig. 2). On the basis of the weight loss from the pure  $\text{Li}_2\text{CO}_3$ , we estimate that the precipitate (1 mg) comprised  $790 \mu\text{g Li}_2\text{CO}_3$ , and that the remainder was probably composed of residual organic reactants and products, and carbon and/or hydrocarbon species formed during the reaction.

On the basis of XPS, GC-FID and TGA–MS data of the carbonate species, we estimated that a large volume of  $\text{CO}_2$  gas was consumed during the doping process. To calculate how much gas was involved, we

considered the amount of generated  $\text{Li}_2\text{CO}_3$  and deduced that 51% of the LiTFSI participated in the precipitation reaction. The estimated doping efficiency of spiro-OMeTAD was therefore approximately 33%; 51% of the LiTFSI was consumed and the mole ratio of spiro-OMeTAD to LiTFSI was 6 to 4. We note that the doping efficiency (around 11%) estimated from the UV-visible absorption spectrum (Supplementary Fig. 4) was different from the doping efficiency estimated by LiTFSI consumption (Fig. 2f). We attribute this difference to the presence of the additive 4-*tert*-butylpyridine (tBP), which can de-dope oxidized spiro-OMeTAD molecules<sup>38</sup>. After the  $\text{CO}_2$ -bubbling process, tBP remains in the solution, and it probably also remains in the film given that its vapour pressure is as low as  $0.5 \pm 0.4 \text{ mm Hg}$  at  $25^\circ\text{C}$ <sup>39</sup>; this is much lower than the values of other solvents in the solution, such as chlorobenzene (11.97 mm Hg at  $25^\circ\text{C}$ )<sup>39</sup> and acetonitrile (88.50 mm Hg at  $25^\circ\text{C}$ )<sup>39</sup>. Although tBP is essential to prevent phase separation of spiro-OMeTAD and LiTFSI in the mixture<sup>40</sup>, it seems to be detrimental to the doping efficiency. Further investigation will be required to determine the exact role of tBP.

Although  $\text{O}_2$  doping of spiro-OMeTAD under ambient conditions has been extensively studied,  $\text{CO}_2$  doping is—to our knowledge—unexplored, and an appropriate mechanism has therefore not been identified. When a pristine spiro-OMeTAD:LiTFSI blend solution (Fig. 3a) is bubbled with  $\text{CO}_2$  gas under UV light, the photoexcited electrons in the LUMO of spiro-OMeTAD are captured by  $\text{CO}_2$ . The negatively charged  $\text{CO}_2$  (or radical anion) can now react with the lithium ions<sup>41</sup>, producing  $\text{Li}_2\text{CO}_3$  and carbon species (Fig. 3b). During the reaction, spiro-OMeTAD can be oxidized into radical cations and/or diradical dications, forming stabilized radicals with  $\text{TFSI}^-$  (ref.<sup>9</sup>) (Fig. 3c). This mechanism is similar to what has previously been reported for  $\text{O}_2$  p-type doping, in which the negatively charged gaseous species reacts with the metal ion, resulting in metal oxide precipitates.

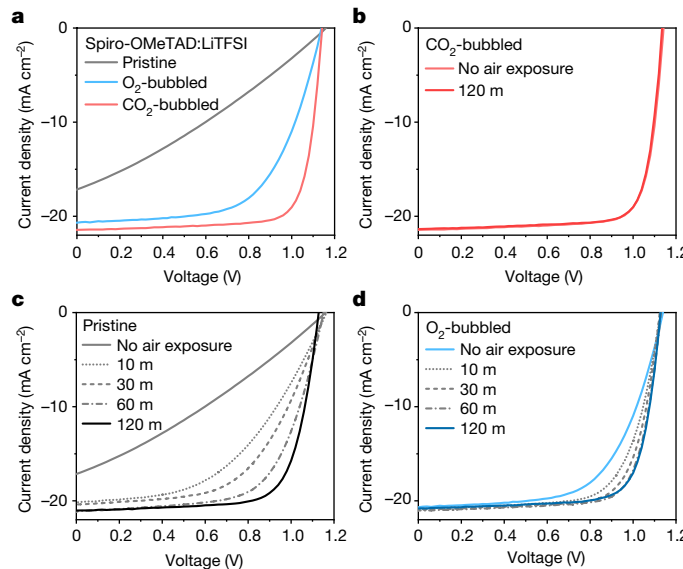


**Fig. 4 | Performance of perovskite solar cells using pristine and gas-treated hole conductors.** **a–d**,  $J$ – $V$  characteristics of perovskite solar cells using a pristine,  $\text{O}_2$ -treated, and  $\text{CO}_2$ -treated spiro-OMeTAD:LiTFSI film as the hole-conducting layer. **b–d**, Changes in  $J$ – $V$  characteristics of solar cells with  $\text{CO}_2$ -treated (b), pristine (c) and  $\text{O}_2$ -treated (d) spiro-OMeTAD:LiTFSI upon exposure to air.

## Solar cells with $\text{CO}_2$ -doped spiro-OMeTAD:LiTFSI

Next, we fabricated perovskite solar cells incorporating  $\text{CO}_2$ -treated spiro-OMeTAD:LiTFSI films as the HTL, and compared them to solar cells using pristine and  $\text{O}_2$ -treated spiro-OMeTAD:LiTFSI films. The solar cell containing a pristine spiro-OMeTAD:LiTFSI film showed poor device performance, exhibiting a power conversion efficiency (PCE) of 9.02% (open-circuit voltage  $V_{\text{OC}} = 1.16 \text{ V}$ , short-circuit current density  $J_{\text{SC}} = 17.7 \text{ mA cm}^{-2}$  and fill factor FF = 0.44) (Fig. 4a, Supplementary Table 1). The solar cell with an  $\text{O}_2$ -treated spiro-OMeTAD:LiTFSI film showed an improved device performance, yet had a limited efficiency of 17.3% ( $V_{\text{OC}} = 1.14 \text{ V}$ ,  $J_{\text{SC}} = 20.9 \text{ mA cm}^{-2}$  and FF = 0.74) (Fig. 4a, Supplementary Table 2). By contrast, the solar cell containing a  $\text{CO}_2$ -treated spiro-OMeTAD:LiTFSI film as an HTL reached a PCE of 19.1% ( $V_{\text{OC}} = 1.14 \text{ V}$ ,  $J_{\text{SC}} = 21.2 \text{ mA cm}^{-2}$  and FF = 0.79). This is slightly higher than the PCE of 18.3% (Supplementary Table 3) that was obtained from a solar cell using a two-metal-salt approach, which also avoids the need for air

exposure by adding tris(2-(1H-pyrazol-1-yl)-4-tert-butylpyridine) cobalt(III) tri[bis(trifluoromethane)sulfonimide] (FK209 Co(III)TFSI salt) to the blend.

In the conventional post-processing doping scheme, the spiro-OMeTAD:LiTFSI films are exposed to air for several hours, or sometimes overnight depending on ambient conditions<sup>8,9,42</sup>. For the solar cells using CO<sub>2</sub>-bubbled spiro-OMeTAD:LiTFSI, no additional efficiency enhancement was found after post-process exposure to air (Fig. 4b, Extended Data Fig. 3, Supplementary Fig. 3), whereas for the solar cells with the pristine (Fig. 4c, Extended Data Fig. 4, Supplementary Fig. 4) and the O<sub>2</sub>-bubbled (Fig. 4d, Extended Data Fig. 5, Supplementary Fig. 5) spiro-OMeTAD:LiTFSI, the PCEs gradually increased during air exposure, reaching a maximum after 2 h and 1 h of air exposure, respectively (Supplementary Tables 1, 2). The observed increase in PCE is mainly related to conductivity enhancements of the spiro-OMeTAD films<sup>43</sup>. The CO<sub>2</sub>-bubbled spiro-OMeTAD:LiTFSI exhibits a conductivity ( $4.91 \times 10^{-5} \text{ S cm}^{-1}$ ) approximately 100 times higher than that of pristine spiro-OMeTAD ( $6.04 \times 10^{-7} \text{ S cm}^{-1}$ ), and around 5 times higher than that of O<sub>2</sub>-bubbled spiro-OMeTAD:LiTFSI ( $1.04 \times 10^{-5} \text{ S cm}^{-1}$ ) (Extended Data Fig. 6a). Although the conventional air-exposure process enhances the conductivity of pristine spiro-OMeTAD:LiTFSI films<sup>44,45</sup> (Extended Data Fig. 6b), it is still lower than that of the CO<sub>2</sub>-treated film ( $1.86 \times 10^{-5} \text{ S cm}^{-1}$ ). Moreover, we found that the defect density at the surfaces and/or interfaces of the solar cell containing a CO<sub>2</sub>-treated spiro-OMeTAD:LiTFSI film ( $5.41 \times 10^{15} \text{ cm}^{-3}$ ) is considerably lower than that obtained from the solar cell with a pristine spiro-OMeTAD:LiTFSI ( $3.86 \times 10^{16} \text{ cm}^{-3}$ ) (Supplementary Fig. 6a). In the solar cells using pristine and O<sub>2</sub>-bubbled spiro-OMeTAD:LiTFSI, the defect densities after the conventional air-exposure process decreased from  $3.86 \times 10^{16} \text{ cm}^{-3}$  to  $7.02 \times 10^{15} \text{ cm}^{-3}$  and from  $1.67 \times 10^{16} \text{ cm}^{-3}$  to  $6.94 \times 10^{15} \text{ cm}^{-3}$ , respectively (Supplementary Fig. 6a–c). The solar cell using CO<sub>2</sub>-treated spiro-OMeTAD:LiTFSI showed a negligible change in defect density (Supplementary Fig. 6a, d).

## Removal of Li ions improves device reliability

We investigated how reducing the density of lithium ions in the HTL affects the overall reliability of the device. The CO<sub>2</sub>-bubbling process produces relatively stable Li<sub>2</sub>CO<sub>3</sub> salts, which are insoluble and can be readily filtered out. First, from TOF-SIMS 2D elemental mapping, we clearly observed that lithium ions formed clusters of a few hundred micrometres in size in a pristine spiro-OMeTAD:LiTFSI film (Extended Data Fig. 7a). By contrast, the CO<sub>2</sub>-treated spiro-OMeTAD:LiTFSI film showed a large reduction in the density of lithium ions (Extended Data Fig. 7b), verifying that the majority of the detrimental lithium ions were removed by filtration. Second, we also conducted TOF-SIMS depth profiling to show how reducing the content of lithium ions in the HTL lowered the overall content in the vertical device direction. For the solar cell with a pristine spiro-OMeTAD:LiTFSI HTL, a strong signal corresponding to lithium ions was detected throughout the active layer and both charge-extraction layers. Lithium ions intercalating into the perovskite active layer can result in decomposition of the perovskite and formation of metallic lead<sup>12,46</sup>, creating recombination sites. The lithium ions were concentrated in particular in the bottom contact layers (Extended Data Fig. 8a), which has been shown to result in device failure<sup>44,47</sup>. Similar elemental depth profiles were found for the solar cell with a spiro-OMeTAD:LiTFSI:FK209 HTL (Extended Data Fig. 8b). Notably, in the solar cell with a CO<sub>2</sub>-doped spiro-OMeTAD:LiTFSI HTL, the lithium ion signal decreased by 1–2 orders of magnitude, and little accumulation of lithium ions in the bottom contact layers was found (Extended Data Fig. 8c).

Using maximum power point (MPP) tracking (Supplementary Fig. 7), we estimated how the decrease in the number of lithium ions affects the reliability of the device. The MPP for a control cell with a pristine spiro-OMeTAD:LiTFSI HTL decreased to below 65% of its initial value

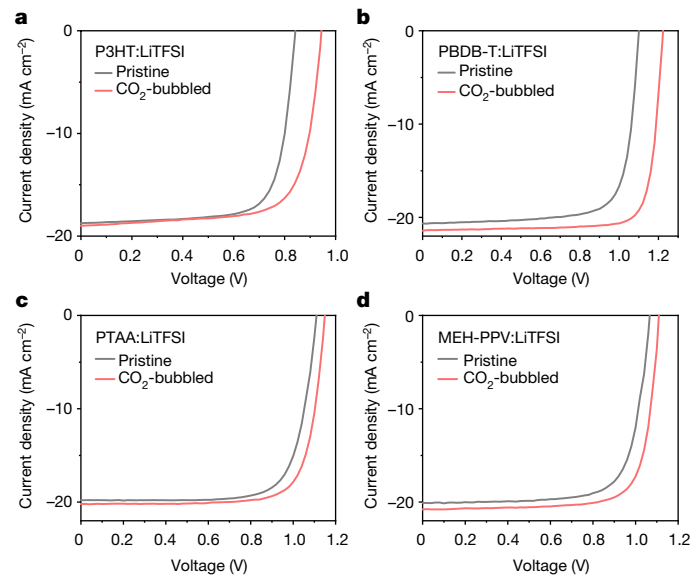


**Fig. 5 | Performance of perovskite solar cells using pristine or CO<sub>2</sub>-doped polymer interlayers.** a–d, J–V characteristics of perovskite solar cells using P3HT:LiTFSI (a), PBDB-T:LiTFSI (b), PTAA:LiTFSI (c) and MEH-PPV:LiTFSI (d), with and without the CO<sub>2</sub>-doping process.

within 6 h (Extended Data Fig. 9). Another control cell, containing a spiro-OMeTAD:LiTFSI:FK209 HTL, also showed a rapid decrease in maximum power, to a value less than 75% of its initial MPP after 6 h (Extended Data Fig. 9). By contrast, the perovskite solar cell containing CO<sub>2</sub>-doped spiro-OMeTAD:LiTFSI showed a much slower decrease in MPP, retaining approximately 80% of its initial maximum power even after 500 h of MPP tracking (Extended Data Fig. 9). We therefore attribute the improvement in device reliability to reduced amounts of Li ions in the solar cells containing CO<sub>2</sub>-doped spiro-OMeTAD:LiTFSI HTLs.

## CO<sub>2</sub>-doped π-conjugated polymers

Finally, we used CO<sub>2</sub> to dope the following representative conjugated polymers: poly(3-hexylthiophene-2,5-diyl) (P3HT), poly[[4,8-bis[5-(2-ethylhexyl)-2-thienyl]benzo[1,2-b:4,5-b']dithiophene-2,6-diyl]-2,5-thiophenediyl][5,7-bis(2-ethylhexyl)-4,8-dioxo-4H,8H-benzo[1,2-c:4,5-c']dithiophene-1,3-diyl]] (PBDB-T), poly[bis(4-phenyl)(2,4,6-trimethylphenyl) amine] (PTAA) and poly[2-methoxy-5-(2-ethylhexyloxy)-1,4-phenylenevinylene] (MEH-PPV). CO<sub>2</sub> doping enhanced the conductivity of the polymers by at least a factor of two and by up to two orders of magnitude (Extended Data Fig. 10a–d), which was supported by photoluminescence quenching studies<sup>48</sup> (Supplementary Fig. 8a–d). Perovskite solar cells fabricated using CO<sub>2</sub>-treated polymer HTLs exhibited enhanced PCEs (Fig. 5, Supplementary Table 4): from 11.5% to 13.0% (P3HT); from 17.3% to 22.1% (PBDB-T); from 16.7% to 18.0% (PTAA) and from 16.0% to 17.8% (MEH-PPV). These improvements in efficiency are mostly attributed to enhanced values of FF and V<sub>OC</sub>, which are to be expected when the conductivity of charge-extraction layers is increased<sup>48–50</sup>.

In summary, we have demonstrated the feasibility of doping small-molecule and polymeric organic semiconductors with CO<sub>2</sub> for use as HTLs in perovskite solar cells. CO<sub>2</sub> rapidly oxidizes the semiconductor by obtaining electrons; the negatively charged CO<sub>2</sub> gas then reacts with lithium ions, forming carbonates that can be easily filtered out of the solution before use. We showed that the CO<sub>2</sub>-doping process rapidly enhances the conductivity of the HTL, yielding reliable, high-efficiency perovskite solar cells without the need for any post-processing using air and light. This doping process reduces the fabrication time of the device by several hours, while simultaneously removing potentially detrimental compounds from the solar cell.

## Online content

Any methods, additional references, Nature Research reporting summaries, source data, extended data, supplementary information, acknowledgements, peer review information; details of author contributions and competing interests; and statements of data and code availability are available at <https://doi.org/10.1038/s41586-021-03518-y>.

1. Hawash, Z., Ono, L. K. & Qi, Y. B. Recent advances in spiro-MeOTAD hole transport material and its applications in organic–inorganic halide perovskite solar cells. *Adv. Mater. Interfaces* **5**, 1700623 (2018).
2. Bach, U. et al. Solid-state dye-sensitized mesoporous TiO<sub>2</sub> solar cells with high photon-to-electron conversion efficiencies. *Nature* **395**, 583–585 (1998).
3. Green, M. A., Ho-Baillie, A. & Snaith, H. J. The emergence of perovskite solar cells. *Nat. Photon.* **8**, 506–514 (2014).
4. Tan, H. R. et al. Efficient and stable solution-processed planar perovskite solar cells via contact passivation. *Science* **355**, 722–726 (2017).
5. Saliba, M. et al. Cesium-containing triple cation perovskite solar cells: improved stability, reproducibility and high efficiency. *Energy Environ. Sci.* **9**, 1989–1997 (2016).
6. Lee, C. P., Li, C. T. & Ho, K. C. Use of organic materials in dye-sensitized solar cells. *Mater. Today* **20**, 267–283 (2017).
7. Cho, A. N. & Park, N. G. Impact of interfacial layers in perovskite solar cells. *ChemSusChem* **10**, 3687–3704 (2017).
8. Cappel, U. B., Daeneke, T. & Bach, U. Oxygen-induced doping of spiro-MeOTAD in solid-state dye-sensitized solar cells and its impact on device performance. *Nano Lett.* **12**, 4925–4931 (2012).
9. Abate, A. et al. Lithium salts as “redox active” p-type dopants for organic semiconductors and their impact in solid-state dye-sensitized solar cells. *Phys. Chem. Chem. Phys.* **15**, 2572–2579 (2013).
10. Wang, S., Yuan, W. & Meng, Y. S. Spectrum-dependent spiro-OMeTAD oxidation mechanism in perovskite solar cells. *ACS Appl. Mater. Interfaces* **7**, 24791–24798 (2015).
11. Nguyen, W. H., Bailie, C. D., Unger, E. L. & McGehee, M. D. Enhancing the hole-conductivity of spiro-OMeTAD without oxygen or lithium salts by using spiro(TFSI)<sub>2</sub> in perovskite and dye-sensitized solar cells. *J. Am. Chem. Soc.* **136**, 10996–11001 (2014).
12. Tan, B. et al. LiTFSI-free spiro-OMeTAD-based perovskite solar cells with power conversion efficiencies exceeding 19%. *Ad. Energy Mater.* **9**, 1901519 (2019).
13. Boyd, C. C., Cheacharoen, R., Leijtens, T. & McGehee, M. D. Understanding degradation mechanisms and improving stability of perovskite photovoltaics. *Chem. Rev.* **119**, 3418–3451 (2019).
14. van Reenen, S., Vitorino, M. V., Meskers, S. C. J., Janssen, R. A. J. & Kemerink, M. Photoluminescence quenching in films of conjugated polymers by electrochemical doping. *Phys. Rev. B* **89**, 205206 (2014).
15. Bard, A. J. & Faulkner, L. R. *Electrochemical Methods: Fundamentals and Applications* (Wiley, 2000).
16. Cardona, C. M., Li, W., Kaifer, A. E., Stockdale, D. & Bazan, G. C. Electrochemical considerations for determining absolute frontier orbital energy levels of conjugated polymers for solar cell applications. *Adv. Mater.* **23**, 2367–2371 (2011).
17. Xu, B. et al. Tailor-making low-cost spiro[fluorene-9,9'-xanthene]-based 3D oligomers for perovskite solar cells. *Chem* **2**, 676–687 (2017).
18. Benson, E. E., Kubiaik, C. P., Sathrum, A. J. & Smieja, J. M. Electrocatalytic and homogeneous approaches to conversion of CO<sub>2</sub> to liquid fuels. *Chem. Soc. Rev.* **38**, 89–99 (2009).
19. Speight, J. *Lange's Handbook of Chemistry* 16th edn, Ch. 2 (McGraw-Hill Education, 2005).
20. Chase, M. W. *NIST-JANAF Thermochemical Tables* 4th edn (American Institute of Physics, 1998).
21. Macdiarmid, A. G., Mammone, R. J., Kaner, R. B. & Porter, S. J. The concept of doping of conducting polymers: the role of reduction potentials. *Philos. Trans. R. Soc. A* **314**, 3–15 (1985).
22. Forward, R. L. et al. Protocol for quantifying the doping of organic hole-transport materials. *ACS Energy Lett.* **4**, 2547–2551 (2019).
23. Shirono, K., Morimatsu, T. & Takemura, F. Gas solubilities (CO<sub>2</sub>, O<sub>2</sub>, Ar, N<sub>2</sub>, H<sub>2</sub>, and He) in liquid chlorinated methanes. *J. Chem. Eng. Data* **53**, 1867–1871 (2008).
24. IUPAC. *Solubility Data Series* Vol. 7, 311 (Pergamon, 1981).
25. IUPAC. *Solubility Data Series* Vol. 50, 257 (Pergamon, 1992).
26. Koppenol, W. H. & Rush, J. D. Reduction potential of the CO<sub>2</sub>/CO<sub>2</sub><sup>·-</sup> couple. A comparison with other Cl radicals. *J. Phys. Chem.* **91**, 4429–4430 (1987).
27. Armstrong, D. A. et al. Standard electrode potentials involving radicals in aqueous solution: inorganic radicals (IUPAC Technical Report). *Pure Appl. Chem.* **87**, 1139–1150 (2015).
28. Zhu, Z., Shi, X., Fan, G., Li, F. & Chen, J. Photo-energy conversion and storage in an aprotic Li-O<sub>2</sub> battery. *Angew. Chem. Int. Ed.* **58**, 19021 (2019).
29. Gittleman, F. S. et al. Raman spectroscopy in lithium-oxygen battery systems. *ChemElectroChem* **2**, 1446–1457 (2015).
30. Ryu, W. H. et al. Heme biomolecule as redox mediator and oxygen shuttle for efficient charging of lithium-oxygen batteries. *Nat. Commun.* **7**, 12925 (2016).
31. Edström, K., Gustafsson, T. & Thomas, J. O. The cathode–electrolyte interface in the Li-ion battery. *Electrochim. Acta* **50**, 397–403 (2004).
32. Deng, X. Y. et al. Surface chemistry of Cu in the presence of CO<sub>2</sub> and H<sub>2</sub>O. *Langmuir* **24**, 9474–9478 (2008).
33. Favaro, M. et al. Subsurface oxide plays a critical role in CO<sub>2</sub> activation by Cu(111) surfaces to form chemisorbed CO<sub>2</sub>, the first step in reduction of CO<sub>2</sub>. *Proc. Natl. Acad. Sci. USA* **114**, 6706–6711 (2017).
34. Feng, N. N., He, P. & Zhou, H. S. Critical challenges in rechargeable aprotic Li-O<sub>2</sub> batteries. *Adv. Energy Mater.* **6**, 1502303 (2016).
35. Xie, J. F., Liu, Q., Huang, Y. Y., Wu, M. X. & Wang, Y. B. A porous Zn cathode for Li-CO<sub>2</sub> batteries generating fuel-gas CO. *J. Mater. Chem. A* **6**, 13952–13958 (2018).
36. Ma, S. Y. et al. Tailoring the components and morphology of discharge products towards highly rechargeable Li-CO<sub>2</sub>/CO<sub>2</sub> batteries. *Chem. Commun.* **54**, 8072–8075 (2018).
37. Strehle, B., Solchenbach, S., Metzger, M., Schwenke, K. U. & Gasteiger, H. A. The effect of CO<sub>2</sub> on alkyl carbonate trans-esterification during formation of graphite electrodes in Li-ion batteries. *J. Electrochem. Soc.* **164**, A2513–A2526 (2017).
38. Lamberti, F. et al. Evidence of spiro-OMeTAD de-doping by tert-butylpyridine additive in hole-transporting layers for perovskite solar cells. *Chem* **5**, 1806–1817 (2019).
39. Yaws, C. L. & Satyro, M. A. in *The Yaws Handbook Of Vapor Pressure: Antoine Coefficients* 2nd edn (ed. Yaws, C. L.) Ch. 1 (Gulf, 2015).
40. Wang, S. et al. Role of 4-tert-butylpyridine as a hole transport layer morphological controller in perovskite solar cells. *Nano Lett.* **16**, 5594–5600 (2016).
41. Liu, B. et al. Recent advances in understanding Li-CO<sub>2</sub> electrochemistry. *Energy Environ. Sci.* **12**, 887–922 (2019).
42. Liu, G. L., Xi, X., Chen, R. L., Chen, L. P. & Chen, G. Q. Oxygen aging time: a dominant step for spiro-OMeTAD in perovskite solar cells. *J. Renew. Sustain. Energy* **10**, 043702 (2018).
43. An, Y. et al. Perovskite solar cells: optoelectronic simulation and optimization. *Sol. RRL* **2**, 1800126 (2018).
44. Schloemer, T. H., Christians, J. A., Luther, J. M. & Sellinger, A. Doping strategies for small molecule organic hole-transport materials: impacts on perovskite solar cell performance and stability. *Chem. Sci.* **10**, 1904–1935 (2019).
45. Hawash, Z., Ono, L. K. & Qi, Y. B. Moisture and oxygen enhance conductivity of LiTFSI-doped spiro-MeOTAD hole transport layer in perovskite solar cells. *Adv. Mater. Interfaces* **3**, 1600117 (2016).
46. Dawson, J. A. et al. Mechanisms of lithium intercalation and conversion processes in organic–inorganic halide perovskites. *ACS Energy Lett.* **2**, 1818–1824 (2017).
47. Li, Z. et al. Extrinsic ion migration in perovskite solar cells. *Energy Environ. Sci.* **10**, 1234–1242 (2017).
48. Stoltzfus, M. et al. Approaching the fill factor Shockley–Queisser limit in stable, dopant-free triple cation perovskite solar cells. *Energy Environ. Sci.* **10**, 1530–1539 (2017).
49. Le Corre, V. M. et al. Charge transport layers limiting the efficiency of perovskite solar cells: how to optimize conductivity, doping, and thickness. *ACS Appl. Energy Mater.* **2**, 6280–6287 (2019).
50. Luo, D. Y., Su, R., Zhang, W., Gong, Q. H. & Zhu, R. Minimizing non-radiative recombination losses in perovskite solar cells. *Nat. Rev. Mater.* **5**, 44–60 (2020).

**Publisher's note** Springer Nature remains neutral with regard to jurisdictional claims in published maps and institutional affiliations.

© The Author(s), under exclusive licence to Springer Nature Limited 2021, corrected publication 2021

## Methods

### Chemicals and reagents

Perovskite precursor compounds (formamidinium iodide (FAI) (Greatcell Solar), methylammonium bromide (MABr) (Greatcell Solar), caesium iodide (CsI) (99.999%, Sigma-Aldrich), lead iodide ( $PbI_2$ ) (99.99%, trace metals basis, TCI Chemicals), lead bromide ( $PbBr_2$ ) (98%, Sigma-Aldrich)), materials for charge transporting layers ( $TiCl_4$  (99.9%, Sigma-Aldrich), KOH (ACS reagent, ≥85%, pellets, Sigma-Aldrich), spiro-OMeTAD (99%, Sigma-Aldrich), P3HT (weight-averaged molecular mass  $M_w = 50,000\text{--}70,000$ , Rieke Metals), PBDB-T ( $M_w \geq 70,000$ , Brilliant Matters), PTAA (number-averaged molecular mass  $M_n = 7,000\text{--}10,000$ , Sigma-Aldrich), MEH-PPV ( $M_w > 100,000$ , Lumtec), LiTFSI (99.95% trace metals basis, Sigma-Aldrich), FK 209 Co(III)TFSI (98% trace metals basis, Sigma-Aldrich)), and solvents [*N,N*-dimethylformamide (DMF) (anhydrous, 99.8%, Sigma-Aldrich), dimethyl sulfoxide (DMSO) (99+, Alfa Aesar), chlorobenzene (anhydrous, 99.8%, Sigma-Aldrich), chloroform (≥99.5%, Sigma-Aldrich), benzyl alcohol (anhydrous, 99.8%, Sigma-Aldrich), diethyl ether (anhydrous, ≥99.7%, Sigma-Aldrich), acetonitrile (anhydrous, 99.8%, Sigma-Aldrich), 4-*tert*-butylpyridine (98%, Sigma-Aldrich), methanol (AmericanBio), ethanol (Macron), acetone (Decon), hexane (Sigma-Aldrich)) were purchased from the stated chemical vendors and were used as received without further purification.

### Synthesis of chlorine-capped $TiO_2$ nanocrystals

To obtain chlorine-capped  $TiO_2$  ( $TiO_2\text{-Cl}$ ) nanocrystals for the electron transporting layer we followed a procedure reported elsewhere<sup>4</sup>. In brief,  $TiCl_4$  (4 ml) was slowly injected into 16 ml of cold anhydrous ethanol, yielding a yellow solution. Anhydrous benzyl alcohol (80 ml) was added to the solution, and the mixture was stirred for 10 min. After the addition of benzyl alcohol, the solution turned red. The solution was then transferred to an oven and stored at 85 °C for 12 h. To enable the precipitation of  $TiO_2$  nanocrystals in the solution, diethyl ether was added.  $TiO_2$  nanocrystals were collected by centrifugation at 5,000 rpm for 2 min. The collected  $TiO_2$  nanocrystals were subsequently washed with anhydrous ethanol and diethyl ether and dried under vacuum for 12 h. To obtain a  $TiO_2\text{-Cl}$  colloidal solution (around 5 mg ml<sup>-1</sup>), the dried  $TiO_2$  nanocrystal powder was combined with a solvent mixture of anhydrous chloroform and anhydrous methanol (1:1 volume ratio). The final dispersion was sonicated for 2 h before use.

### Preparation of organic semiconductor solutions

To prepare a spiro-OMeTAD:LiTFSI solution, 65 mg of spiro-OMeTAD was dissolved in 1 ml of chlorobenzene, and 20 µl of tBP and 70 µl of LiTFSI solution (170 mg of LiTFSI in 1 ml of acetonitrile) were added into the spiro-OMeTAD solution. For CO<sub>2</sub>-doped spiro-OMeTAD, the mixed solution was bubbled with CO<sub>2</sub> under UV light for 1 min. For the MPP measurements, a more concentrated solution of spiro-OMeTAD:LiTFSI was prepared. Spiro-OMeTAD (100 mg) was dissolved in 1.1 ml of chlorobenzene, and 40 µl of LiTFSI solution (574 mg of LiTFSI in 1 ml of acetonitrile) and 35 µl of tBP were added into the neat spiro-OMeTAD solution. To apply the CO<sub>2</sub> doping process to a more concentrated spiro-OMeTAD:LiTFSI solution, the solution was prepared with a small amount of tBP (5 µl) because tBP tends to reduce the oxidized spiro-OMeTAD. In addition, extra UV exposure and a stabilization step were needed. For example, after the 1-min CO<sub>2</sub> bubbling, the solution was kept under UV light for an additional 30 min, and stored in an N<sub>2</sub>-filled glovebox for at least 6 h before use. The rest of the tBP (30 µl ml<sup>-1</sup>) was added to the stock solution and the final solution was filtered before use. For the co-doped spiro-OMeTAD solution, FK 209 Co(III)TFSI was added as an additional metal salt together with LiTFSI. Spiro-OMeTAD (100 mg) was dissolved in 1.1 ml of chlorobenzene. In the neat spiro-OMeTAD solution, 23 µl of LiTFSI solution (540 mg of LiTFSI in 1 ml of acetonitrile), 10 µl of FK 209 Co(III)TFSI solution (376 mg of FK

209 Co(III)TFSI in 1 ml of acetonitrile), and 39 µl of tBP were added<sup>51</sup>. To prepare the polymer solutions, we slightly modified a protocol found in the literature for the preparation of a PTAA solution<sup>52</sup>, and used the same amounts of tBP and LiTFSI that had been used for preparation of the spiro-OMeTAD solution. For the P3HT solution, 20 mg of P3HT was dissolved in 1 ml of chlorobenzene, and 7.5 µl of tBP and 15 µl of LiTFSI solution (170 mg of LiTFSI in 1 ml of acetonitrile) were added into the polymer solution. For the PBDB-T solution, we added 10 mg of PBDB-T in 1 ml of chlorobenzene. In the polymer solution, 3.3 µl of tBP and 7.5 µl of LiTFSI solution were added. To prepare the PTAA solution, 10 mg of PTAA was dissolved in 1 ml of chloroform, and 3.3 µl of tBP and 7.5 µl of LiTFSI solution were added into the polymer solution. For the MEH-PPV solution, we added 5 mg of MEH-PPV in 1 ml of toluene, and 1.6 µl of tBP and 3.3 µl of LiTFSI solution were added in the solution. All solutions were prepared in a nitrogen-filled glovebox, and were kept in the glovebox until the CO<sub>2</sub> bubbling process was performed.

### Gas bubbling and filtration

Two syringe needles were stuck into the vial through a PTFE/silicone septum, with one syringe needle used as a gas inlet connected to a CO<sub>2</sub> (or O<sub>2</sub>) gas cylinder, and the other syringe needle used as the outlet. The bubbling rate was around 2 ml s<sup>-1</sup>. While the solution was bubbled with CO<sub>2</sub>, we used a UV flashlight (UV301D, maximum 3,000 mW, 365 nm) to illuminate the solution for 1 min. No changes in volume or concentration were observed after the bubbling process. The gas-bubbled solutions were filtered with PTFE hydrophobic filters (pore size ≈ 0.22 µm), and the filtered solutions were used for HTLs. No filter was used for polymer solutions.

### GC-FID measurement

Gas mixture in the headspace was analysed by gas chromatography (SRI 8610C, Multiple Gas Analyzer #1) equipped with a flame ionization detector (FID) via syringe injection (250 µl). Ultrahigh-purity Ar (99.999%) was used as the carrier gas.

### Collection of lithium carbonate

Bubbling the spiro-OMeTAD:LiTFSI solution with CO<sub>2</sub> produces two reaction products: oxidized spiro-OMeTAD and lithium carbonate (Li<sub>2</sub>CO<sub>3</sub>). The oxidized spiro-OMeTAD can be re-dissolved in the chlorobenzene-based reaction solution after CO<sub>2</sub> bubbling, but Li<sub>2</sub>CO<sub>3</sub> is precipitated in the solution because the metal carbonate is insoluble in chlorobenzene. To collect Li<sub>2</sub>CO<sub>3</sub> from the solution after the CO<sub>2</sub>-bubbling process, we filtered the resulting solution with a PTFE hydrophobic filter (0.22 µm pore). The collected precipitate was rinsed with chlorobenzene and acetonitrile three times. The filter catching the precipitate was placed under vacuum for 12 h to dry residual solvents, and the white powder was collected. The powder was stored in an argon glovebox until the TGA-MS measurement was performed.

### A powder form of CO<sub>2</sub>-doped spiro-OMeTAD

After CO<sub>2</sub> bubbling and filtration, the filtered solution can be directly spin-coated on the perovskite layer for HTL formation. Alternatively, the reaction product can be collected as a solid powder to facilitate handling and storage for a longer period. To do this, we changed the solvent from chlorobenzene to chloroform. Besides the change in solvent, the solution preparation procedure was the same unless otherwise noted. Spiro-OMeTAD (65 mg) is dissolved in chloroform, and 20 µl of tBP and 70 µl of LiTFSI solution (170 mg of LiTFSI in 1 ml of acetonitrile) were added in the chloroform solution. The spiro-OMeTAD:LiTFSI solution was bubbled with CO<sub>2</sub> under UV light illumination for 1 min. The resulting solution was filtered using a filter with pore size of 0.22 µm and the filtered solution was slowly dripped into a 100 ml hexane bath. A dark brown powder immediately precipitated in the bath. The powder-dispersed solution was centrifuged twice with fresh hexane and the sediment was collected (Supplementary Fig. 9). The collected

# Article

powder was dried in a vacuum oven for 30 min and the dried powder was stored in an argon glovebox. This powder can be directly used as a hole transporting material, or can be used as a dopant for neutral spiro-OMeTAD. This approach is similar to the doping approach using AgTFSI, but does not produce potentially detrimental hygroscopic substances such as silver halides<sup>53</sup> (for example, AgI) from a residue AgTFSI in the HTL.

## TGA–MS measurement

A Discovery TGA (TA Instruments) was used to measure the mass change of samples as they were heated from room temperature to 1,000 °C at a heating rate of 10 °C min<sup>-1</sup> under an argon or an air atmosphere. TGA data acquisition and evaluation, as well as instrument control, were carried out using the TRIOS software package. The evolved gases were analysed with a Discovery TGA coupled to the Discovery MS by means of a stainless-steel transfer line, which was kept at a constant temperature of 300 °C to avoid gas condensation in a capillary. Data was acquired using the mass spectrometer software Processes Eye, triggered by the TGA system.

## Fabrication of planar perovskite solar cells

Pre-patterned indium tin oxide (ITO)-coated glass substrates were sequentially cleaned using deionized water, acetone and isopropanol. ETLs were deposited on the cleaned ITO substrates by spin casting a TiO<sub>2</sub>–Cl solution at the rate of 3,000 rpm for 20 s. The TiO<sub>2</sub>–Cl-coated substrates were annealed on a hot plate at 150 °C for 30 min in air. The TiO<sub>2</sub>–Cl-coated substrates were rinsed with a KOH solution (0.01 M in deionized water) and dried at 100 °C for 5 min. After drying, the substrates were transferred into a nitrogen-filled glovebox to deposit perovskite layers and HTLs. A Cs<sub>0.05</sub>FA<sub>0.81</sub>MA<sub>0.14</sub>PbI<sub>2.55</sub>Br<sub>0.45</sub> precursor solution (1.2 M) was prepared in the solvent mixture of DMF (800 µl) and DMSO (200 µl). A one-step spin coating procedure was applied for formation of the perovskite layer. While the perovskite solution was spin-coated on the ETL-coated substrate, 150 µl of chlorobenzene was dripped 5 s before the end of spinning procedure (4,000 rpm, 20 s). After coating the perovskite layer, the substrate was placed on a preheated hotplate (100 °C) for 10 min. After cooling the substrate to room temperature, hole transporting material (HTM) solutions were spin-coated on the dried perovskite layers. For spiro-OMeTAD-based HTLs, pristine and doped solutions were spin-coated at 3,500 rpm for 40 s. For polymer-based HTLs, the polymer solutions were spin-coated at 1,000 rpm for 40 s. After the HTL deposition, gold (~50 nm) was deposited using a thermal evaporator (Angstrom Engineering) to form top contacts.

## J–V characteristics of the solar cells

The current density–voltage (*J*–*V*) characteristics were measured using a Keithley 2400 SMU under 1-sun (AM1.5G) irradiance (100 mW cm<sup>-2</sup>), for which a 100 W xenon arc lamp was used with no UV cutoff filter, calibrated by a Newport-certified reference silicon solar cell. The *J*–*V* measurements were carried out in a nitrogen-filled glovebox with a scanning rate of 250 mV s<sup>-1</sup> (voltage step, 100 mV; delay time, 200 ms). The active area of a solar cell is 1.8 mm<sup>2</sup>, defined by a shadow mask during the metal deposition. No further masking was applied.

## Capacitance–voltage characterization

For the Mott–Schottky analysis, the capacitance of the solar cells was measured over applied voltages from 0 V to 1 V at a frequency of 1 kHz with a small AC perturbation of 20 mV. From the slopes of the curve onsets, the densities of surface defects were calculated<sup>54</sup>.

## Conductivity measurement

For the conductivity measurements, silicon substrates were patterned with platinum interdigitated electrodes fabricated at the NYU Tandon Nanofabrication Cleanroom on a 100 cm silicon wafer

(University Wafer) with a 250 nm thermally grown oxide layer. A 20 nm titanium adhesion layer followed by a 200 nm platinum layer was deposited in a physical vapour deposition chamber (Kurt J. Lesker Company). Electrode features were patterned with AZ 5214 E photoresist (Microchemicals GmbH) and SÜSS MicroTec MA 6 Contact Aligner followed by ion beam etching (IntlVac Inc. Nanoquest II). After patterning, wafers were diced into 1 cm<sup>2</sup> square dices with a Disco DAD3320 dicing saw at the City University of New York Advanced Science Research Center. For the spiro-OMeTAD samples, we used the IDE that has 39 pairs of fingers with 3 mm length, 100 µm width and 10 µm spacing. For polymer samples, we used interdigitated electrodes with wider spacing, and 39 pairs of fingers with 3 mm length, 5 µm width and 100 µm spacing were deposited on the chips. On the patterned substrates, hole-transporting materials were spin-coated at the same spinning rates as used to fabricate solar cells in a nitrogen-filled glovebox. The conductivity measurements were conducted with a Bio-Logic VSP potentiostat by applying a voltage from -1 V to +1 V. The conductivity measurements were performed with a Bio-Logic VSP potentiostat by applying a voltage from -1 V to +1 V. The conductivity of the HTMs was calculated according to a reported equation<sup>55</sup>:  $\sigma = \frac{I}{V} \frac{d}{(2n-1)lh}$ , where *I* is the current, *V* is the voltage, *d* is the spacing between adjacent electrodes, *n* is the number of finger pairs, *l* is the length of the inter-digitated fingers and *h* is the film thickness.

## UV–vis–NIR absorption spectroscopy

UV–vis–NIR spectra were measured using a Cary 5000 UV-Vis-NIR instrument.

## Steady-state photoluminescence spectroscopy

Photoluminescence was measured on a Photon Technology International QuantaMaster4 Fluorometer (Horiba). The excitation wavelengths were set at the maximum absorption peaks of spiro-OMeTAD and polymers, and the emission spectra were monitored at around their maximum photoluminescence.

## XPS measurements

The collected precipitate powder was pressed onto a tape and placed in the XPS. The XPS spectra were collected using a monochromatic 1,486.7 eV Al Kα X-ray source on a PHI VersaProbe II X-ray photoelectron spectrometer with a system resolution of 0.47 eV. The energy scale was calibrated using Cu 2p<sub>3/2</sub> (932.67 eV) and Au 4f<sub>7/2</sub> (84.00 eV) peaks on a clean copper plate and a clean gold foil.

## MPP tracking

To track the MPP, we wrote a program based on the perturb and observe method (Supplementary Fig. 7). To facilitate rapid MPP tracking, the program starts from the *V*<sub>oc</sub> and the applied voltage bias is lowered until the voltage reaches MPP. Once it reaches the voltage for MPP, the applied bias is perturbed with a voltage deviation of 0.01 V and the maximum power points are collected every 350 ms. A Keithley 2400 SMU was used to apply a voltage bias and to track the MPP. For the duration of the experiment, continuous light (100 mW cm<sup>-2</sup>, AM1.5G) with no UV cutoff filter illuminated a solar cell without a temperature controller. Raw data, including spikes that might originate from lamp power instability, was presented.

## TOF-SIMS

TOF-SIMS (Physical Electronics NanoTOF) was used to obtain two-dimensional ion maps and depth profiles of samples. Two-dimensional ion mapping for spiro-OMeTAD:LiTFSI composite films was conducted using a 30 kV Bi<sup>+</sup> liquid metal ion gun (LMIG) and analysing positive secondary ions across a 500 µm × 500 µm area. The ion depth profiles of interest were measured by sputtering perovskite solar cells using a 3 kV Ar gas gun (500 nA current, rastered over a 1,000 µm × 1,000 µm area) followed by probing the composition

of the rastered surface using a 30 kV Bi<sup>+</sup> LMIG and analysing positive secondary ions across a 50 μm × 50 μm area. For each sputter–probe cycle, samples were sputtered for 5 s.

## Computation

Computational investigations were performed using the ab initio quantum chemistry calculation method implemented by the Gaussian 16 simulation package<sup>56</sup> with the PM6 semi-empirical method for initial screening and the B3LYP level/6-311+G(d,p) basis set for geometry optimization. A maximum of 3 × (number of atoms – 1) structures were generated by the Monte Carlo sampling method for initial screening, and the Packmol open source package<sup>57</sup> was used to find the initial configuration of the molecule clusters<sup>58</sup>.

## Data availability

The data that support the findings of this study are available from the corresponding author upon reasonable request. Source data are provided with this paper.

## Code availability

The codes used for this study are available from the corresponding author upon reasonable request.

51. Kim, G. et al. A thermally induced perovskite crystal control strategy for efficient and photostable wide-bandgap perovskite solar cells. *Sol. RRL* **4**, 2000033 (2020).
52. Lee, J. et al. A printable organic electron transport layer for low-temperature-processed, hysteresis-free, and stable planar perovskite solar cells. *Adv. Energy Mater.* **7**, 1700226 (2017).
53. Kato, Y. et al. Silver iodide formation in methyl ammonium lead iodide perovskite solar cells with silver top electrodes. *Adv. Mater. Interfaces* **2**, 1500195 (2015).
54. Almora, O., Aranda, C., Mas-Marza, E. & Garcia-Belmonte, G. On Mott–Schottky analysis interpretation of capacitance measurements in organometal perovskite solar cells. *Appl. Phys. Lett.* **109**, 173903 (2016).

55. Snow, A. W., Barger, W. R., Klusty, M., Wohtjen, H. & Jarvis, N. L. Simultaneous electrical-conductivity and piezoelectric mass measurements on iodine-doped phthalocyanine Langmuir–Blodgett films. *Langmuir* **2**, 513–519 (1986).
56. Frisch, M. J. et al. *Gaussian 16 Rev. C.01* (Gaussian Inc., 2016).
57. Martínez, L., Andrade, R., Birgin, E. G. & Martínez, J. M. PACKMOL: a package for building initial configurations for molecular dynamics simulations. *J. Comput. Chem.* **30**, 2157–2164 (2009).
58. Kim, D. Y. et al. Ni-stabilizing additives for completion of Ni-rich layered cathode systems in lithium-ion batteries: an ab initio study. *J. Power Sources* **418**, 74–83 (2019).

**Acknowledgements** We acknowledge the National Science Foundation NSF-PECASE award (CBET-0954985) and New York University for partial support of this work. J.K. acknowledges support from the National Research Foundation of Korea (NRF) grant funded by the Korea government (MSIT) (2021R1A2C1008968, 2020R1A6A1A03038697); J.M. from the China Scholarship Council and F.A. from the NSF Fellowship program. This research used resources of the NYU Tandon Nanofabrication Cleanroom & Shared Instrumentation Facilities, and the Center for Functional Nanomaterials (CFN), which is a US DOE Office of Science Facility at Brookhaven National Laboratory under contract no. DE-SC0012704.

**Author contributions** J.K. conceived the project, and it was supervised by A.D.T. J.K. and Y.S. designed the experiments. J.K. and J.A.R. discussed and analysed data. J.K. prepared samples and devices for XPS, C–V, J–V and conductivity studies, and conducted the measurements. J.K. and J.M. fabricated and measured solar cells. Y.W. and Hailiang Wang conducted GC-FID measurements. J.K. and Hang Wang prepared the samples for TGA–MS analysis. Y.S. and D.Y.K. carried out the DFT calculations. G.K., J.K., S.K. and K.L. set up the MPP tracking experiments and J.K. conducted them. A.K., T.S. and M.A.M. patterned electrodes for conductivity measurements. E.C. and J.R.K. set up the photoluminescence measurement system, and J.K., Hang Wang, E.C. and F.A. conducted photoluminescence measurements. T.-D.L. performed ToF-SIMS analysis. Hang Wang provided details for the reactions involving O<sub>2</sub> or CO<sub>2</sub>. J.K., J.A.R. and A.D.T. wrote the draft of the paper, and all authors read and approved the paper.

**Competing interests** J.K., J.A.R., and A.D.T. have filed a PCT patent application.

## Additional information

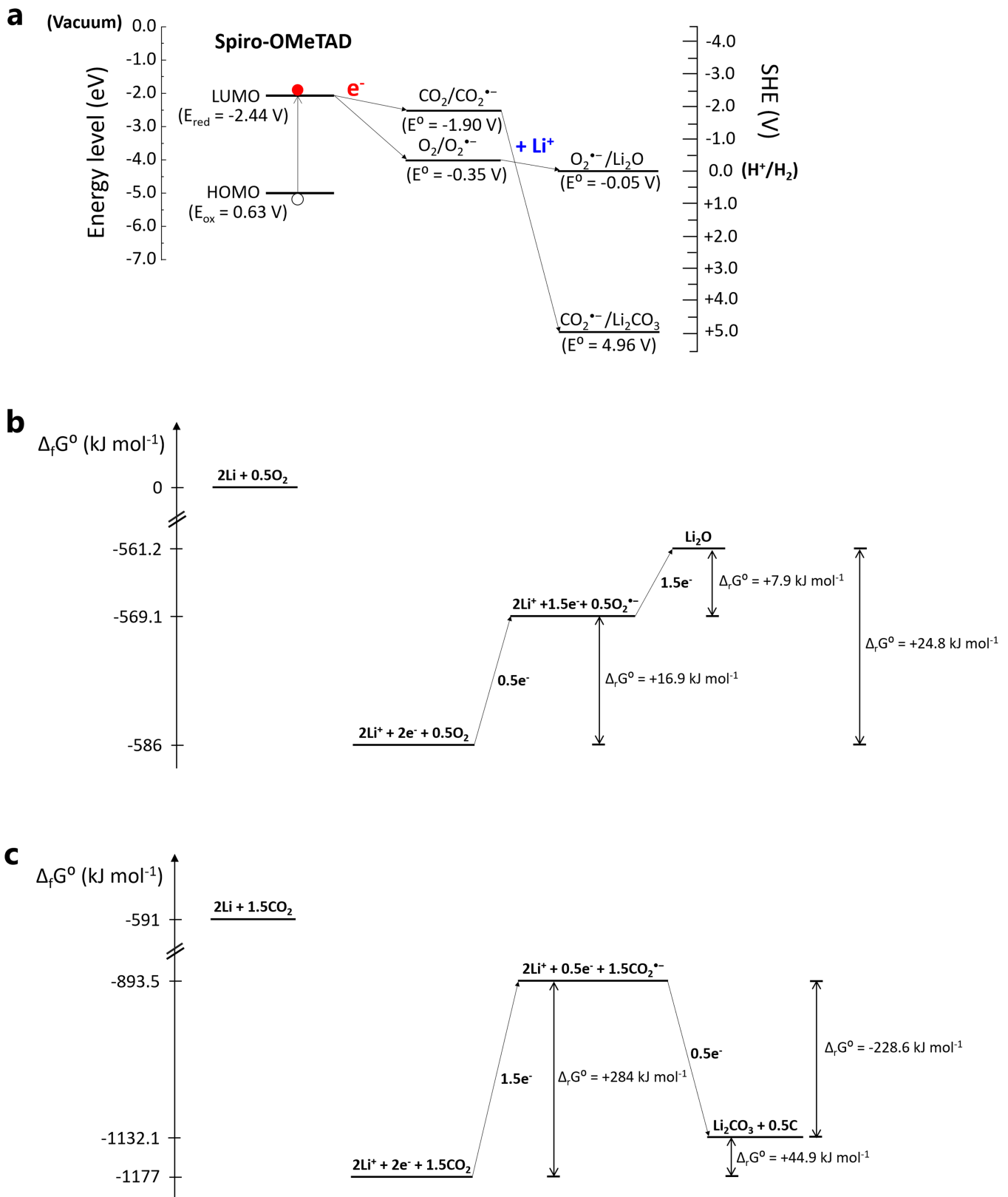
**Supplementary information** The online version contains supplementary material available at <https://doi.org/10.1038/s41586-021-03518-y>.

**Correspondence and requests for materials** should be addressed to A.D.T.

**Peer review information** *Nature* thanks Jianfeng Lu and Tracy Schloemer for their contribution to the peer review of this work.

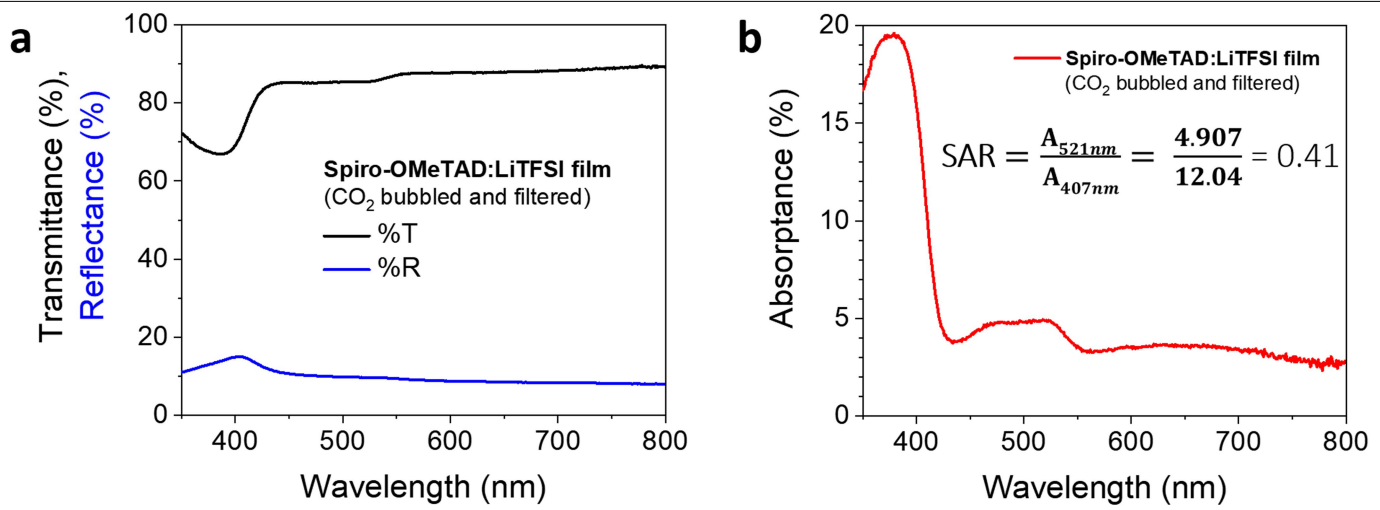
**Reprints and permissions information** is available at <http://www.nature.com/reprints>.

# Article

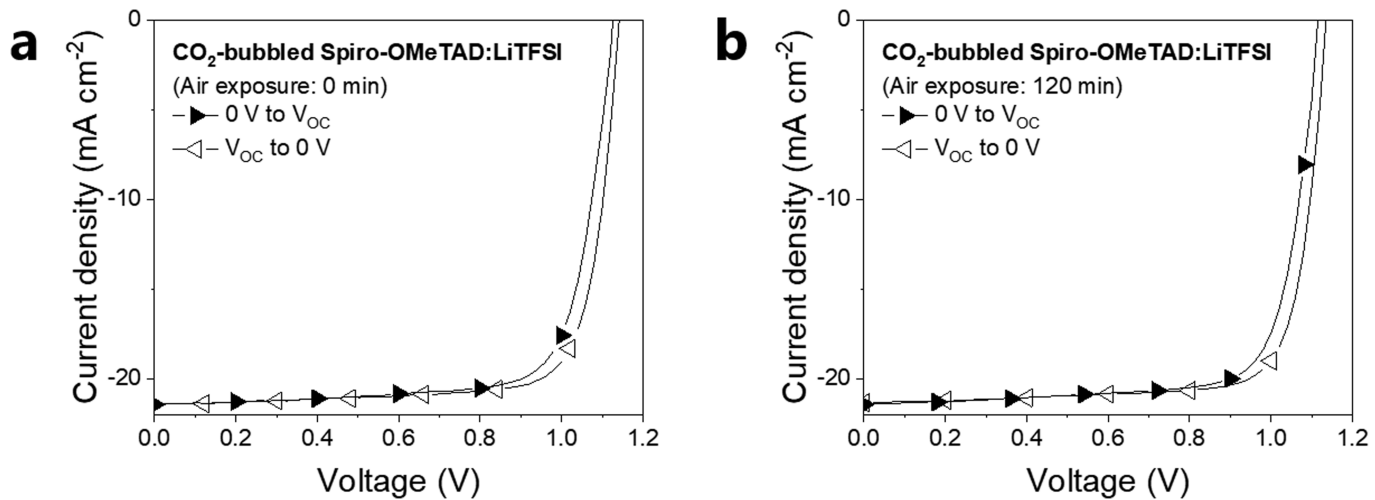


**Extended Data Fig. 1 | Possible doping routes.** **a**, Energy band diagram of spiro-OMeTAD and gas reduction potentials of  $\text{O}_2$  and  $\text{CO}_2$ . Reduced or negatively charged gases will react with lithium ions, producing lithium oxide and carbonate. The HOMO level ( $-5.13 \text{ eV}$ ) of spiro-OMeTAD was estimated from the equation  $E_{\text{HOMO}} = -(E_{\text{ox}} + 4.5 \text{ eV})$ , where the vacuum level ( $E = 0 \text{ eV}$ ) is equivalent to  $-4.5 \text{ V}$  vs SHE<sup>15–17</sup>. The LUMO level ( $-2.05 \text{ eV}$ ) was estimated by

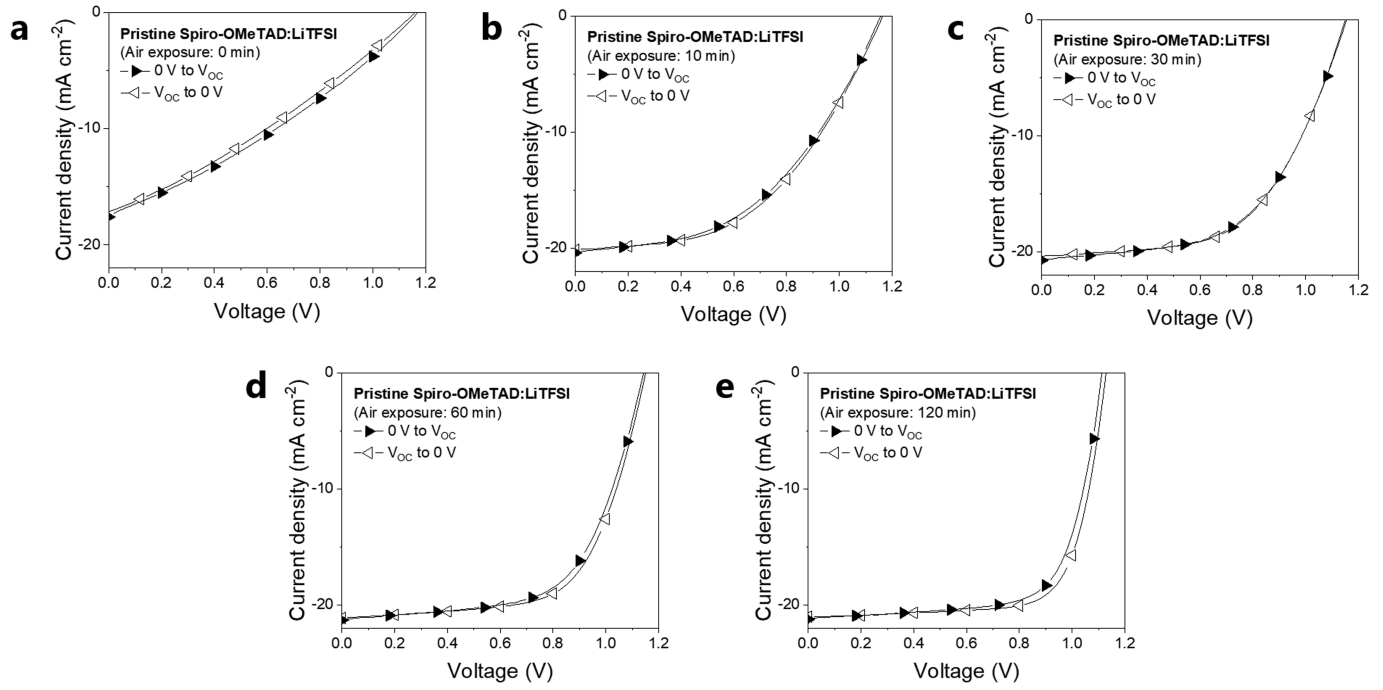
adding the HOMO level and optical band gap ( $E_{\text{gap}}$ )<sup>17</sup>. **b, c**, Possible detailed reaction paths for lithium oxide from the  $\text{O}_2$  bubbling process (**b**) and for lithium carbonate from the  $\text{CO}_2$  bubbling process (**c**). The redox potentials and Gibbs free energy ( $\Delta_f G^\circ$ ) of each reaction are calculated using values from the thermodynamic database<sup>27</sup>.



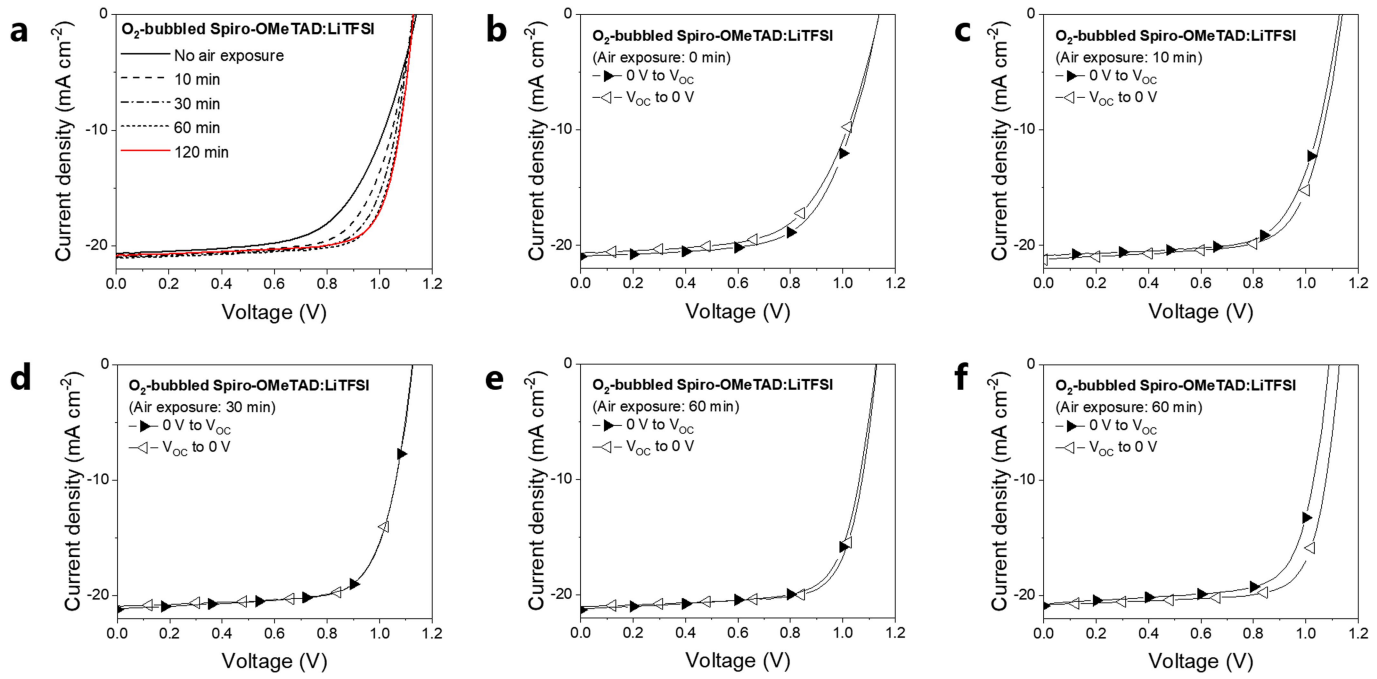
**Extended Data Fig. 2 | Optical data for CO<sub>2</sub>-treated spiro-OMeTAD:LiTFSI.** **a, b**, Transmittance and reflectance (**a**) and absorptance (**b**) spectra of the CO<sub>2</sub>-treated spiro-OMeTAD:LiTFSI film. The standardized absorptance ratio (SAR) is calculated from the ratio of absorptance at 521 nm and 407 nm.



**Extended Data Fig. 3 |  $J$ - $V$  data for a solar cell with a  $\text{CO}_2$ -treated spiro-OMeTAD:LiTFSI HTL before and after air exposure.** **a, b,**  $J$ - $V$  curves of the solar cell before (a) and after (b) air exposure for 120 min.

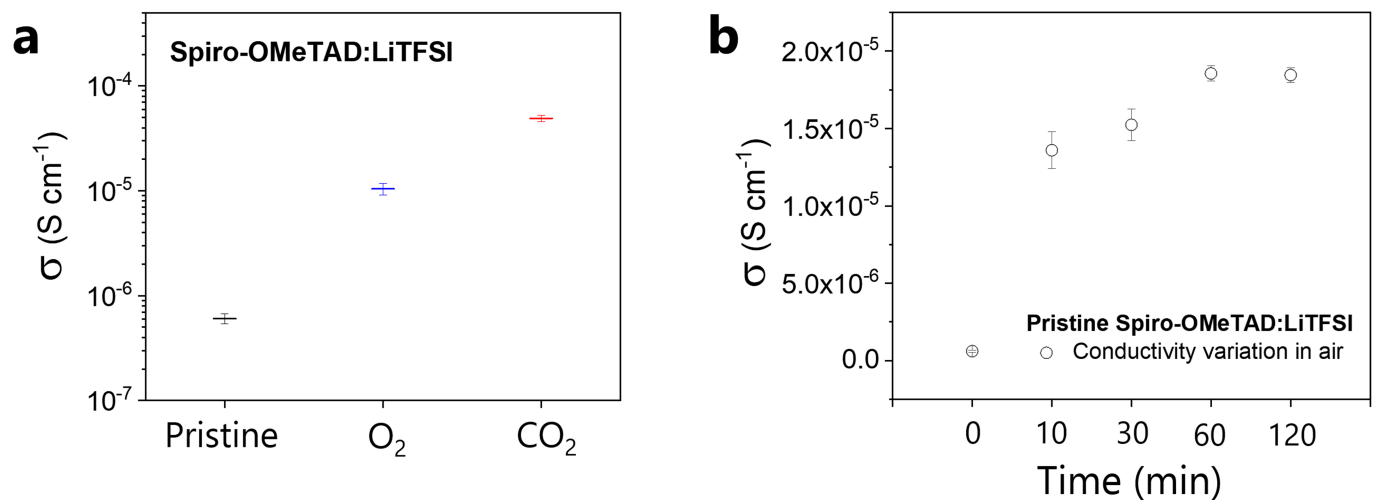


**Extended Data Fig. 4 |  $J$ - $V$  data for a solar cell with a pristine spiro-OMeTAD:LiTFSI HTL before and after air exposure.** a–e,  $J$ - $V$  curves of the solar cell upon exposure to air for 0 min (a), 10 min (b), 30 min (c), 60 min (d) and 120 min (e).



**Extended Data Fig. 5 |  $J$ - $V$  data for a solar cell with an  $\text{O}_2$ -treated spiro-OMeTAD:LiTFSI HTL before and after air exposure. a**, Summary of evolution of the  $J$ - $V$  curve of the solar cell upon exposure to air. **b–e**, Separate  $J$ - $V$  data for

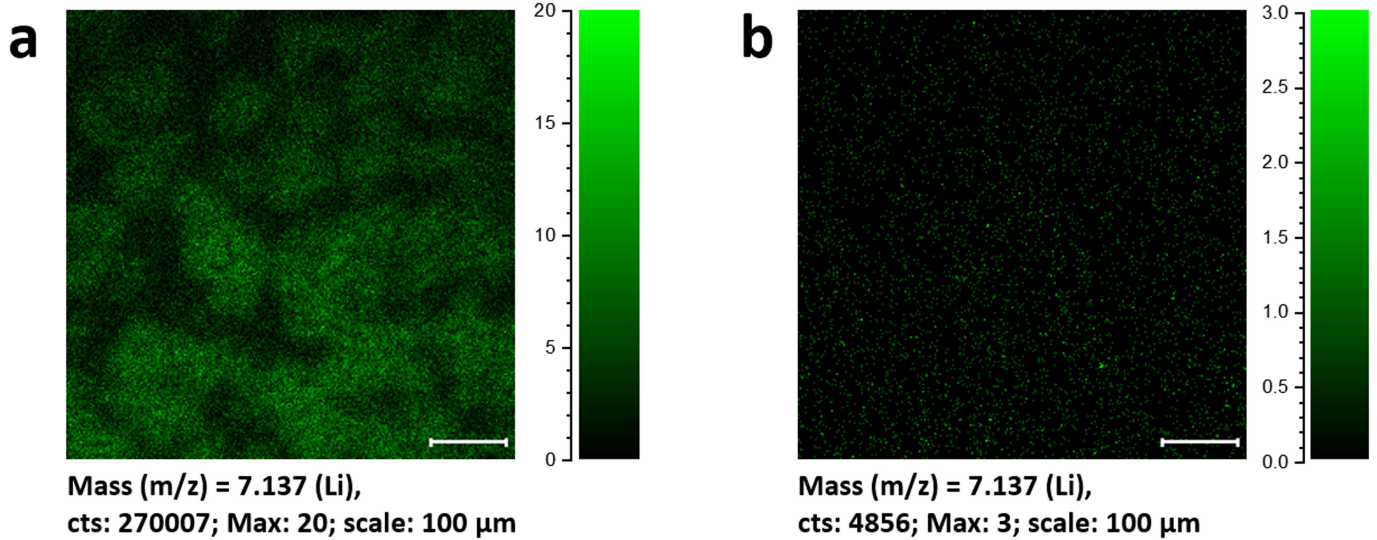
the solar cell upon exposure to air for 0 min (b), 10 min (c), 30 min (d), 60 min (e) and 120 min (f).



**Extended Data Fig. 6 | Changes in the electrical conductivity of spiro-OMeTAD:LiTFSI films fabricated using pristine,  $\text{O}_2$ - and  $\text{CO}_2$ -bubbled spiro-OMeTAD:LiTFSI solutions, and the conductivity changes of pristine films over time upon exposure to air.** **a**, Electrical conductivities ( $\sigma$ ) of the films

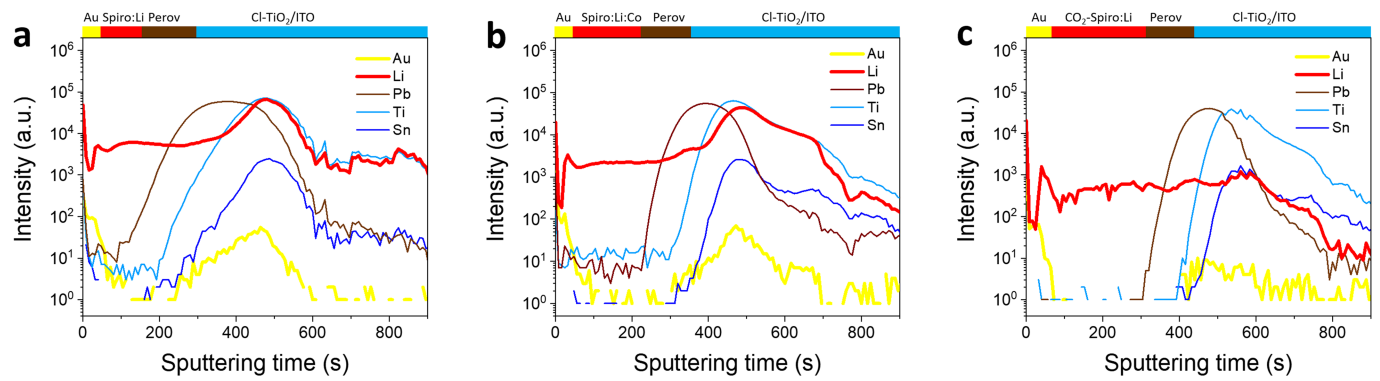
fabricated with pristine,  $\text{O}_2$ -treated and  $\text{CO}_2$ -treated spiro-OMeTAD:LiTFSI solutions. **b**, Electrical conductivity evolution for a pristine spiro-OMeTAD:LiTFSI film in air over time. Central bars or empty circles in the graphs represent average values obtained from 4 samples, and error bars show deviations.

# Article

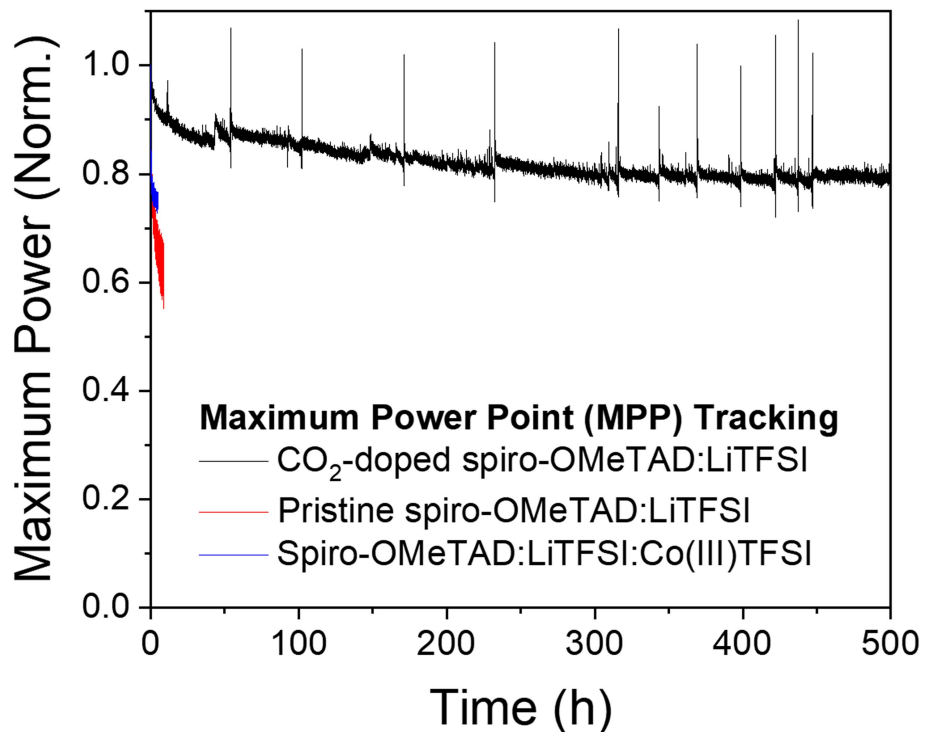


**Extended Data Fig. 7 | TOF-SIMS 2D elemental mapping for Li ion.** Green dots represent Li ions. The scale bar for the Li ion signal intensity in each map was adjusted for the best viewing level. **a**, The density of Li ions is high, forming

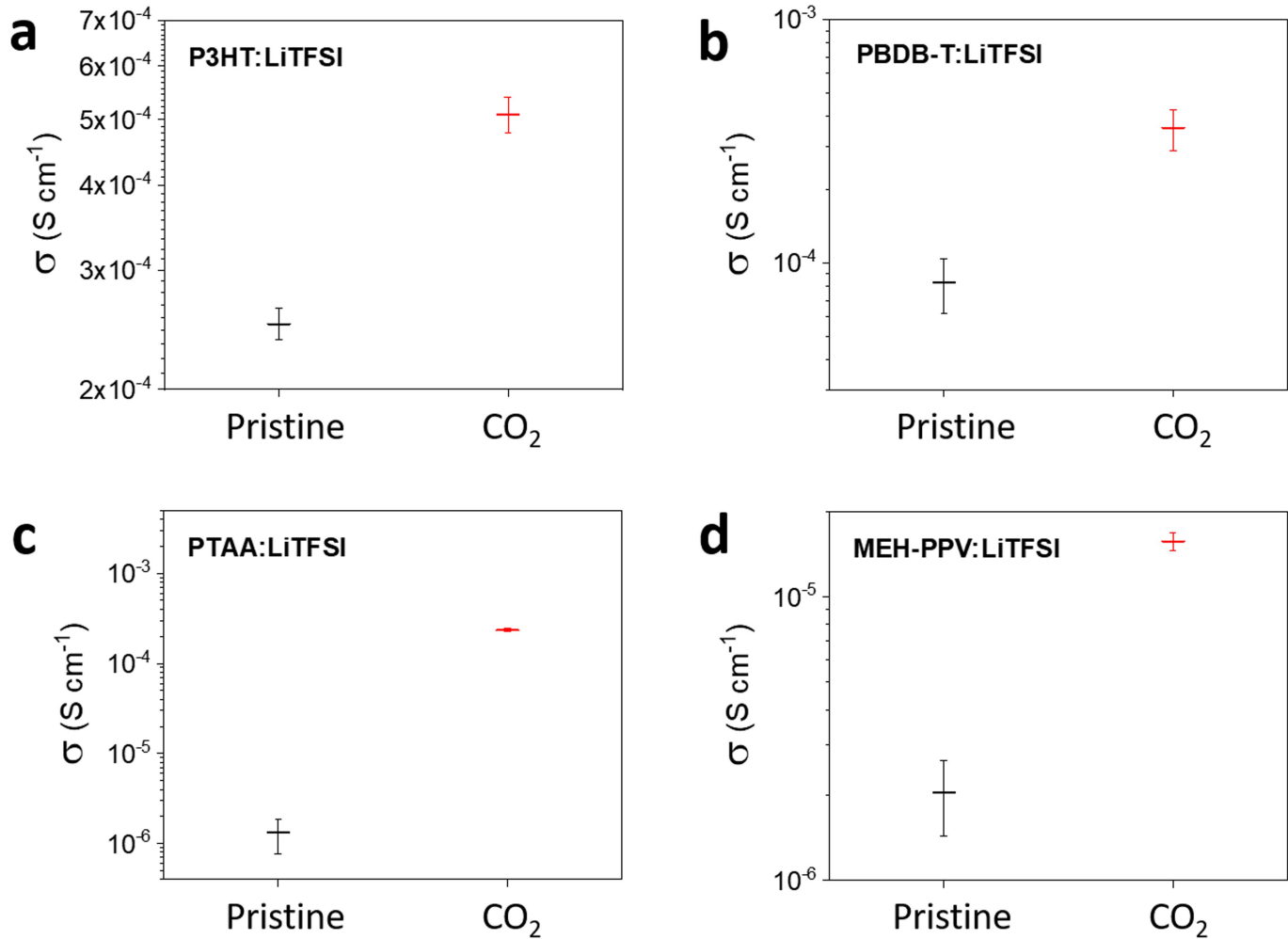
clusters in the pristine spiro-OMeTAD:LiTFSI film. **b**, There are few Li ions in the  $\text{CO}_2$ -treated spiro-OMeTAD:LiTFSI film, because  $\text{Li}_2\text{CO}_3$  precipitate (the doping by-product) was filtered out before film fabrication.



**Extended Data Fig. 8 | TOF-SIMS depth profiles.** **a–c**, Solar cells with a pristine spiro-OMeTAD:LiTFSI HTL (**a**), a spiro-OMeTAD:LiTFSI:Co(III)TFSI HTL (**b**) and a CO<sub>2</sub>-treated spiro-OMeTAD:LiTFSI HTL (**c**).



**Extended Data Fig. 9 | MPP traces for solar cells with pristine spiro-OMeTAD: LiTFSI, spiro-OMeTAD:LiTFSI:Co(III)TFSI, and CO<sub>2</sub>-treated spiro-OMeTAD: LiTFSI as an HTL.** MPP was collected every 350 ms under continuous light illumination (100 mW cm<sup>-2</sup>, AM1.5G) with neither a UV cut-off filter nor a temperature controller. Raw data, including spikes that might originate from a lamp power instability, are presented.



**Extended Data Fig. 10 | Changes in the electrical conductivity of polymer:LiTFSI films with  $\text{CO}_2$  doping.** **a–c**,  $\text{CO}_2$  doping enhances the electrical conductivities of polymer:LiTFSI films that are composed of

P3HT:LiTFSI (a), PBDB-T:LiTFSI (b), PTAA:LiTFSI (c) and MEH-PPV:LiTFSI (d). Central bars or empty circles in the graphs represent average values obtained from 4 samples, and error bars show standard deviations.